A laboratory investigation into rock physics and fracture potential of the Woodford shale, Anadarko Basin, Oklahoma

by

Dustin Matthew Harris

B.S., Juniata College, 2010

A THESIS

Submitted in partial fulfillment of the requirements for the degree

MASTER OF SCIENCE

Department of Geology
College of Arts and Sciences

KANSAS STATE UNIVERSITY
Manhattan, Kansas

2017

Approved by:

Co-Major Professors
Matthew Totten

Approved by:

Co-Major Professors
Abdelmoneam Raef

Copyright

Abstract

The Woodford shale in west-central Oklahoma is an organic and silica rich shale that is a prolific resource play producing gas and liquid hydrocarbons (Gupta et al., 2013). Unconventional shale wells are only producible due to modern hydraulic fracturing techniques. Production surveys from unconventional reservoirs show significant variability between wells and even between fracking stages (Kennedy, 2012). The production potential of a particular shale appears to be related to its brittleness and kerogen content "sweetness". Thus, brittleness analysis becomes important when choosing which shales to produce. A rocks brittleness index can be related directly to elastic properties derived from P- and S-wave velocities, as well as, its specific mineral makeup.

This project's main focus is to determine the elastic rock properties that affect or relate to Woodford shale brittleness and how they relate to the rock's specific mineral makeup and kerogen content. Measurements to determine elastic properties, based on ultrasonic laboratory testing, were conducted on available Woodford cores. The estimated elastic moduli were evaluated via cross-plotting and correlation with a variety of rock properties. Elastic properties are of essential relevance to forward seismic modeling in order to study seismic response. Mineral makeup, determined via XRD and XRF analyses done by Kale Janssen (2017), was used to calculate a mineral-based brittleness index for comparison with the elastic moduli. Evaluation of the elastic moduli assisted in determining which elastic properties directly relate to the brittleness of the shales and, in turn, to geomechanical aspects. These properties were correlated with data from previous studies including mineral percentages, total organic content (TOC), and thermal maturity. These correlations were used to determine which elastic properties best predict

a rock's brittleness index. The calculated brittleness was used to develop a brittleness index map of the Woodford Formation.

Table of Contents

Figures

Tables

Acknowledgments

I would like to thank Dr. Abdelmoneam Raef and Dr. Matt Totten for taking me on as a graduate student and guiding me through this process. I would also like to thank Dr. Michael Lambert for letting me use his Woodford core samples. I would like to thank Dr. Pamela Kempton for being a part of my advisory committee and giving me the opportunity to better myself. I would like to thank Kale Janssen for sharing his XRD and XRF data from the cores with me.

Dedication

I would like to dedicate this work to my friends and family who have been supportive throughout this process. A special thanks to my girlfriend (Andrea) for encouraging me to take on this challenge and sticking with me through it.

I dedicate this work to my fellow K-State Geology Masters Grads., we may have been cheated at IBA but we have graduated anyway

Introduction

With the recent expansion of horizontal drilling and hydraulic fracking, unconventional shale wells have become a very profitable production target in the oil and gas industry. The rise of unconventional shale plays has led to an increase in dry shale gas production in the United States from 1.0 trillion cubic feet in 2006 to 4.8 trillion cubic feet in 2010, about 23 percent of the total natural gas production in the U.S. (EIA, 2011). The Woodford shale formation of the Anadarko Basin has become one of the prime horizontal targets for gas production in Oklahoma accounting for nearly 50 percent of the horizontal wells drilled in 2010 (Fig. 1). Recent developments in hydraulic fracturing and horizontal drilling techniques have played essential roles in the development of the tight oil reservoirs within the Woodford. Knowledge of elastic properties and mineralogical makeup of the shales within this unconventional play are critical to the process of identifying prospective reservoirs that have existing natural fractures or high propensity to develop fracture networks during hydraulic fracturing (Xu and Sonnenberg, 2016).

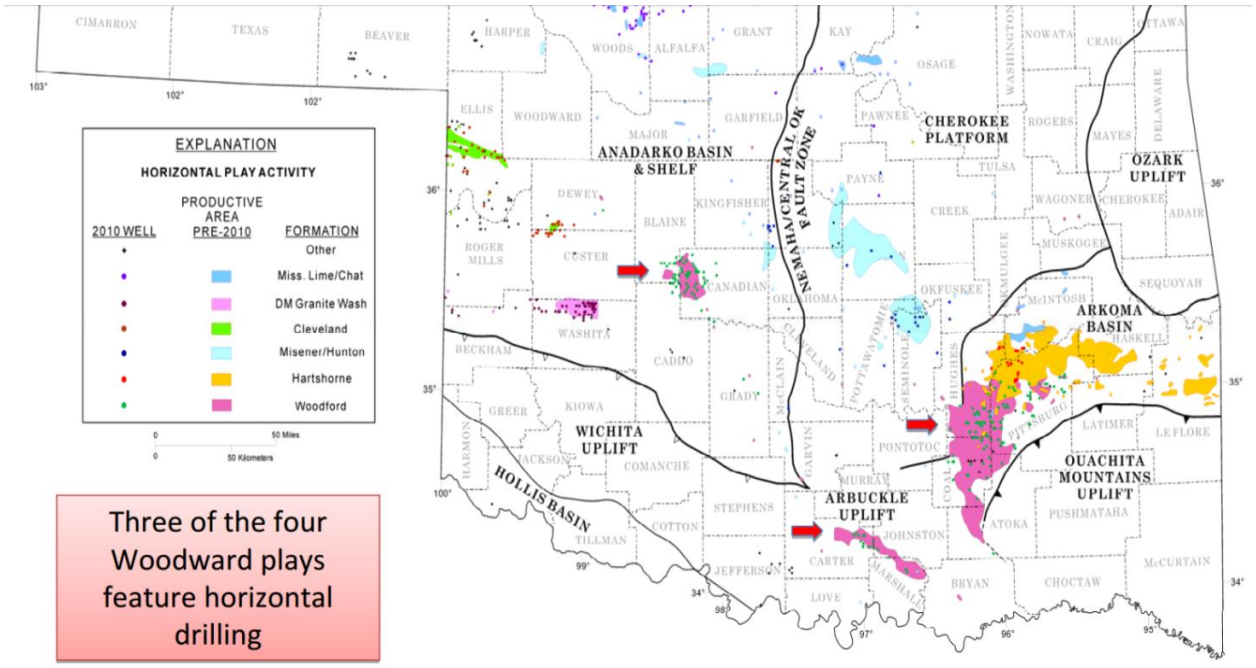

Figure 1. Map of Oklahoma active horizontal drilling plays, 2010. Arrows indicate locations of the 3 Woodford horizontal plays (Oklahoma Geological Survey, 2010).

Assessment of these rock mechanical properties is mainly done by two methods: core measurements taken in a laboratory and petrophysical log analysis. The laboratory core evaluation approach has been used in this study to attain a variety of rock elastic properties. These properties were used to determine both a mineralogical and elastic brittleness index. The total organic content (TOC) and fracture pressure gradient (FG), or brittleness, are critical to the development of any unconventional shale reservoir (Hu et. al, 2015). With brittleness being such an important aspect of unconventional reservoir production, obvious questions still remain. What specific rock properties have the most effect on brittleness? How closely do mineralogical and elastic-based brittleness index calculations relate? Can surface seismic methods be used to evaluate fracability?

For brittleness, rocks are classified into two types by the way they behave under stress: brittle and ductile. It is easier for brittle rocks to develop large complex fracture networks that

enhance production by connecting fracture fairways to the wellbore via hydraulic fracturing (Grieser and Bray, 2007). A multitude of expressions for brittleness index have been proposed to quantify a rocks fracture potential. In this study, two approaches were used to evaluate the brittleness: elastic properties, via Lamé's parameters, and geochemical approach, via XRF analyses that was aided by XRD data, from which a mineralogy is calculated. The XRD and XRF analyses used in this study are from Janssen (2017).

Geologic Setting

Structural History

The Anadarko Basin is a northwest-southeast trending sedimentary structural basin that is of Paleozoic age in western Oklahoma and the Texas Panhandle (Cardott and Lambert, 1982). The early structural history of the Oklahoma Basin region began with the opening of the Tethys Ocean and breakup of Pangaea, which began in the late Precambrian to early Cambrian (Feinstein, 1981). The early Cambrian saw the development of at least two incipient triple junctions in the southeastern United States that combined to initiate a new spreading ridge-transform system. One of the arms of the triple junctions failed, thus extending the rift northwest into the craton (Whitmeyer, 2007). This feature, known as the southern Oklahoma aulacogen, was marked by the intrusion of basic and acidic igneous rocks. Cooling and subsidence resulted in formation of a broader superimposed basin allowing the deposition of a thickened lower Paleozoic sedimentary succession. The subsidence rate decreased by the beginning of the Silurian (Feinstein, 1981). This is indicated by the relatively thing Silurian and Devonian rocks that are of limited lateral extent (Higley, 2014).

The largest early Paleozoic structural features identified in the Anadarko Basin are the northwest-southeast-trending Fort Cobb, Cordell, Sayre, and Mobeetie anticlinal trends. These anticlinal features are believed to have existed prior to the pre-Woodford unconformity that occurred in the Late Devonian time. This is inferred from the absence of the upper Hunton on the anticlines crests as a result of erosion or non-deposition (Fig. 4) (Ball et al., 1991).

The closure of the Iapetus Ocean was first seen in the late Mississippian. The collision of the Laurentia and Gondwana plates gave rise to the Wichita (Pennsylvanian) and Ouchita (Permian) orogenies in the late Paleozoic. This caused the uplift of the Wichita Mountains and Amarillo arch, which include numerous faults, such as Mountain View, Cordell, Cement, Meers, and Duncan-Criner faults, that are along and proximal to the northern boundary of the uplifts (Fig. 2) (Higley, 2014). The Wichita Mountain and Amarillo uplifts were subsequently thrust northward over the southern margin of the southern Oklahoma aulacogen and its basin. Loading caused by the uplifted and overriding north-bound thrust sheets caused renewed subsidence and the Anadarko basin was formed (Fig. 3) (Ball et al, 1991).

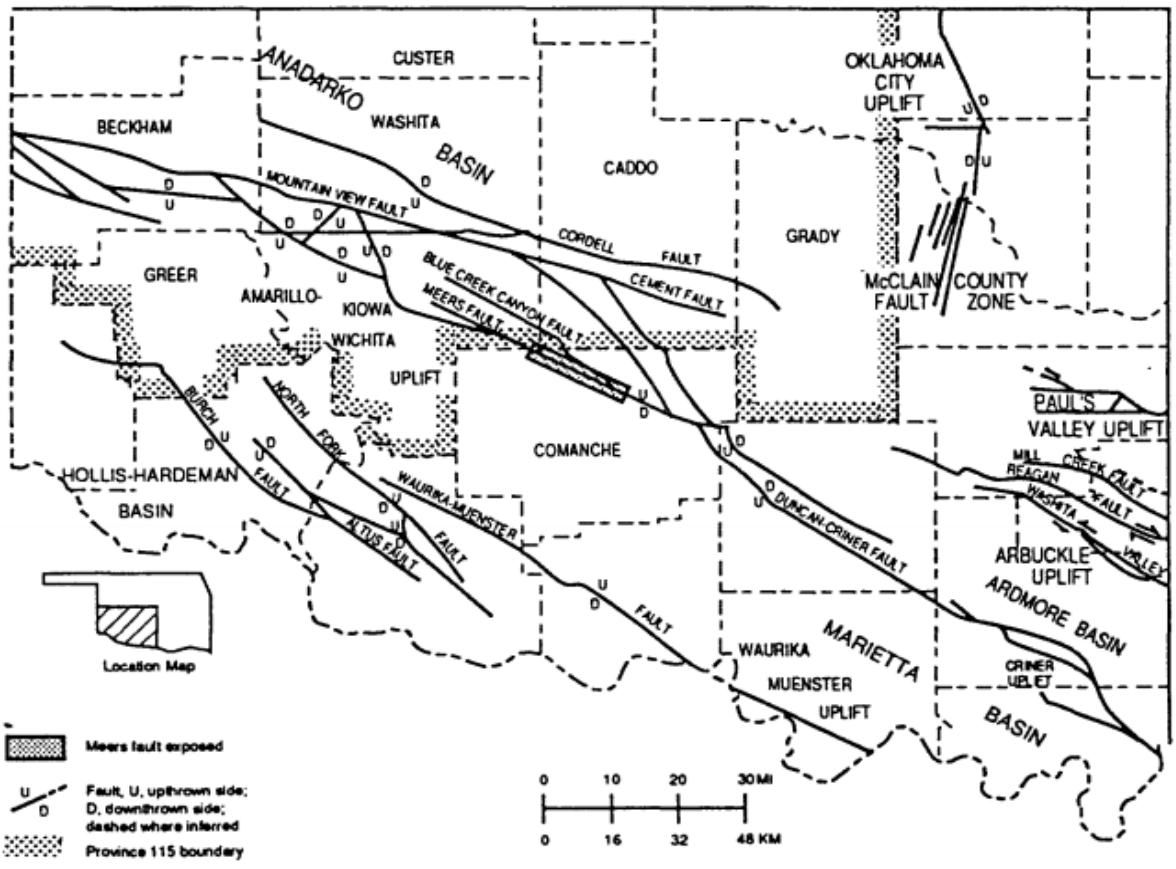

Figure 2. Map of major faults throughout the Anadarko Basin in southwestern Oklahoma (Ball et al., 1991).

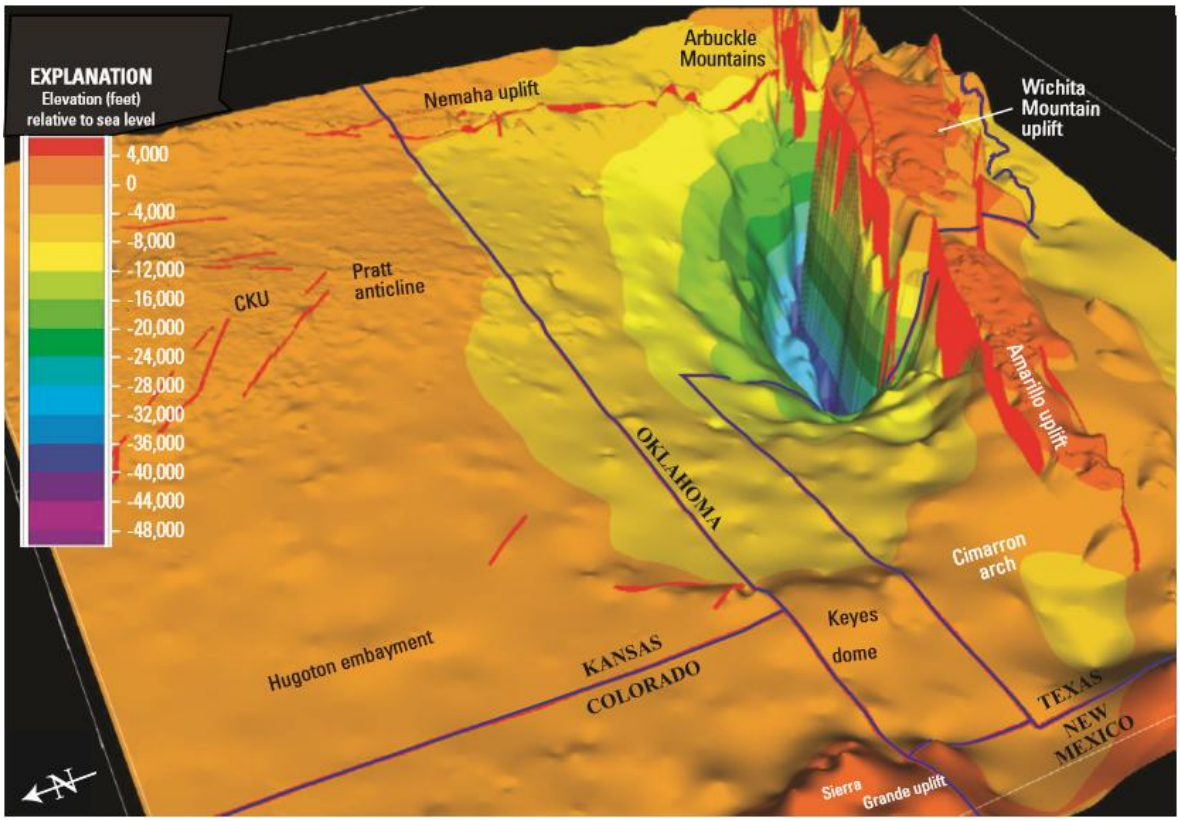

Figure 3. Three-dimensional model of the Anadarko Basin with 18 times vertical exaggeration. Major structures are labeled. Precambrian faults (red) are from Adler and others (1971) (Higley, 2014).

Depositional History

The Anadarko Basin has a range of strata from Cambrian to Permian with minor occurrences of Mesozoic and Cenozoic strata in the northwest. The Silurian-Early Devonian brought about the deposition of the Hunton Group, a shallow marine limestone (Johnson and Cardott, 1992). The Hunton ranges from a clean fossiliferous limestone at the base and top, to argillaceous and silty carbonates in the middle (Johnson and Cardott, 1992). After the deposition of the Hunton a significant uplift and erosion event occurred, which caused the pre-Woodford unconformity (Johnson et al, 1989).

During the Late Devonian to Early Mississippian the basin experienced a major marine transgression that inundated the continental platform, facilitating widespread organic-rich mud accumulation (Rivera et al, 2015). The abundance of organic matter suggests that the Woodford was deposited in anoxic waters. However, a recent study identified that the depositional environments of the Woodford vary between anoxic and suboxic, depending on location and relative paleoenvironmental conditions (Rivera et al, 2015). This variation is reflected in the Woodford with the organic-rich sections likely being deposited during anoxic conditions, while the non organic section were likely deposited during suboxic conditions. The thickness of the shale ranges from nearly zero to upwards of 900 ft throughout the basin. The Misener-Sycamore Sandstones present in the Woodford were the result of the exposed Hunton Group debris being incorporated into the shales (Johnson et al., 1989).

In the Late Early to Middle Mississippian sea levels receded and a warm shallow oxygenated ocean was left. This environment allowed the deposition of a variety of benthic organisms resulting in the formation of a limestone layer above the Woodford. This was followed by further uplift and erosion, as well as periods of orogenesis, during the late Mississippian to Permian period. These events produced the varying stratigraphy and structural features that are present today (Fig. 4) (Coddington, 2013).

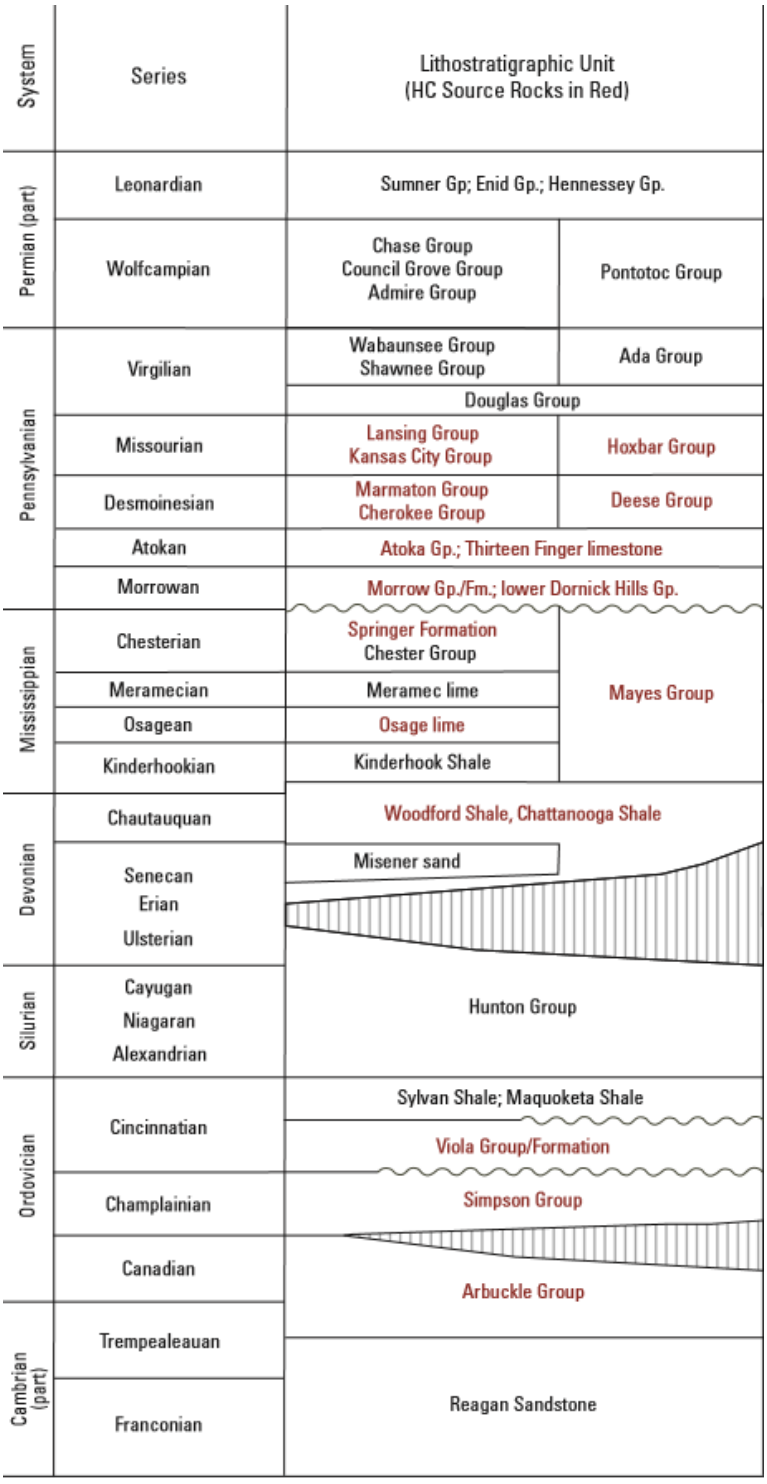

Figure 4. Generalized stratigraphic column for the Anadarko Basin with oil and gas source rocks (red text) (Higley, 2014).

Methodology

Sample Selection

The samples for this study were chosen due to their availability, relevance, and previous research conducted. The samples were originally collected by Dr. Michael Lambert in 1985 from the core library at the OPIC (Oklahoma Petroleum Information Center) in the Oklahoma Geological Survey, as well as, the Kansas Geological Survey. The goal was to obtain samples with a wide spatial distribution throughout the Anadarko Basin and southern Kansas. The core samples were chosen based on their availability and size. A minimum core height of 1 inch was required in order to acquire accurate P- and S-wave velocities through the rock medium, anything thinner would result in high uncertainty in estimating first arrival times. A minimum core width of 1/2 inch was required so that the core covered the entirety of the wave emitting sensors on the platens. If these sensor were not fully covered the P- and S-waves emitted would scatter instead of traveling through the body of the core. A total of 13 samples met the minimum requirements and were chosen for processing (Fig. 5). Seven of the cores are from the middle shale member of the Woodford, one core is from the lower shale member, and five of the cores do not have the shale member recorded.

Figure 5. 13 samples used for geomechanical analysis

The 13 samples were located throughout ten counties in the Anadarko Basin region and three counties in southern Kansas (Tale 1). The samples ranged in depth from approximately 2,170 feet to 14,251 feet (Table 1). The locations for the 13 core samples can be seen depicted in Figure 6 by red markers.

Sample	Name	Latitude	Longitude	Section	Township	Range	County	Depth(ft)	Shale Member
KC06	APC-DEI #1 Goyer	37.4159872	-97.2689981	25	30S	01E	Sumner	3612.2	MSM
KC08	ERDA #1 Bock	38.05301	-93.0706782	15	23S	12E	Greenwood	2170	MSM
KC10	Dalmac #1 Allen	38.58344	-97.69868	7	17S	03W	McPherson	3353.9	MSM
OC02	Texas #1 Gipson	34.0553	-96.64883	11	06S	06E	Marshall	4109	MSM
OC03	Universal #2-16 Dannehl	35.60557	-97.84695	16	13N	06W	Canadian	8620	
OC05	Tenneco #1-11 Edwards	36.30964	-98.66429	11	21N	14W	Garfield	8507.5	MSM
OC06	Huber #1 Cherokee Mehodist	36.71918	-98.38239	21	26N	11W	Alfalfa	6084.5	MSM
OC07	Calvert #2 Bloyd	36.80856	-98.82465	21	27N	15W	Woods	6199.5	MSM
OC08	GHK #1 Hoffman	35.722	-98.8492	1	14N	16W	Custer	14251	LSM
OC10	Heartland #1-2 Wollenburg	34.93407	-97.48863	2	05N	03W	Mcclain	8291	
OC20	Jones #2-B Hall	35.03045	-98.52923	36	07N	13W	Caddo	6158	
OC23	Gomaco #1-2C Allen	unknown	unknown	21	15N	01W	Logan	5626	
OC25	Pan American #1-B Roetzal	36.12142	-98.21657	13	19N	10W	Blaine	8415	

Table 1. Sample locations and their approximate depths.

Figure 6. Oklahoma and southern Kansas county map showing core-sample surface locations (red dots).

Elastic Brittleness

A rock physics analysis was performed on the 13 core samples using the ULT-100, its accompanying ultrasonic velocity software, and a vice system (Fig. 7). The ultrasonic velocity measurements taken were used to study the elastic behavior of the cores at $1/5^{th}$ of in situ, overburden stress conditions. The testing was non-destructive and provided compressional (P)

wave and shear (S) wave first arrival times for each core. These velocities can be used to calculate a variety of dynamic elastic constants such as Poisson's Ratio (u), Young's Modulus (E), Bulk Modulus (K), and Shear Modulus (G).

Figure 7. ULT-100 interface(bottom), ULT-100 P- and S-wave platens(top left), and vice used for in situ simulation (top right).

Prior to processing, each sample's mass, in grams, was measured to one significant figure using a scale. Each sample was then placed in a cylindrical container with water. The original height of the water, with no sample, was measured and an initial volume was calculated using

$V=\pi r^2 h$. Where V is the volume of the cylinder, r is the radius of the cylinder, and h is the original height of the water with no sample. Each sample was then individually placed in the water and the new water height was measured and a second volume was calculated using the same equation. The volume of each specific core was then calculated by simply subtracting the second volume from the original volume: $V_{rock}=V_2-V_1$. After all of the rock volumes were calculated the sample's mass was divided by its volume to get the density of the sample in g/cm^3. This density along with sample height was entered into the GCTS ultrasonic velocity software parameters. The surface area of the platens was also measured in order to calculate an *in situ*, overburden stress. This was done with the use of the equation for the surface area of a circle ($A = \pi r^2$). Lithostatic stress was assumed to increase at one psi per foot of depth. This assumption was made because pressure P is force F per unit area, and according to Newton equation $F=ma$, where *m* is mass and *a* is acceleration. With our interest being in vertical pressure, acceleration would be due to gravity *g*. The mass of a rock normalized to volume is density ρ, and the depth *d* must also be considered. This results in a pressure equation expressed as $P=\rho dg$. As seen in Table 3 the average density of the core samples is approximately $2.15g/cm^3$ or $2150kg/m^3$. A depth of 1 m was assumed and *g* was rounded to 10 to make the math simpler. Plugging these numbers into the equation we get $2150kg/m^3$ x $10m/s^2$ = 21500 pascals(Pa). With 10kPa equaling 1.45psi we get 21500Pa x (1.45psi/10000Pa) = approx 3.12psi/m, and 3.12psi/m is approximately 1 psi/ft when rounded. Thus the surface area was then multiplied by the depth of each core sample in order to get the *in situ*, overburden pressure of the cores. This pressure was applied by squeezing the core between the platens via the vice and was measured using a force gauge applied to the top platen. A majority of these pressures were far too high for the

cores to withstand under the vice without fracturing. Due to these circumstances the samples were run under 1/5 of their *in situ* pressures.

There was a small amount of sample preparation required, in the form of cutting/shaving the cores, due to the need for the cores to be flat on both sides in order to achieve a good air tight coupling with the platens. Before any sample was used, base line data for P- and S-wave travel times between the two platens (face to face time) had to be established. This was done by placing the platens together, under 100lbs of pressure with no sample between them, then sending a P- and S-wave pulse between them. Testing showed that the face to face time for P-waves was 11.5μs and 17.5μs for S-waves. This was necessary in order to later process out the wave propagation time through the platens from the actual core propagation time.

After the samples were run, the GCTS software displayed the results graphically in a plot of voltage vs time (Fig. 8). The raw data were exported to a notepad, then transferred to, and graphed in, Microsoft Excel (2007) in order to more accurately pick first arrival times. The first arrival times were picked from the Excel graphs by evaluating the arrival time of the first peak or trough of the waveform (Fig. 9). This was done for both P- and S-waves separately. The face to face times of each waveform were then subtracted from the chosen first arrival times in order to get the actual arrival times. The calculated first arrival times were converted to seconds, then the height of each specimen was divided by the respective first arrival time, p-arrival for Vp and s-arrival for Vs, in order to get the corresponding P- and S-wave velocities (Table 2).

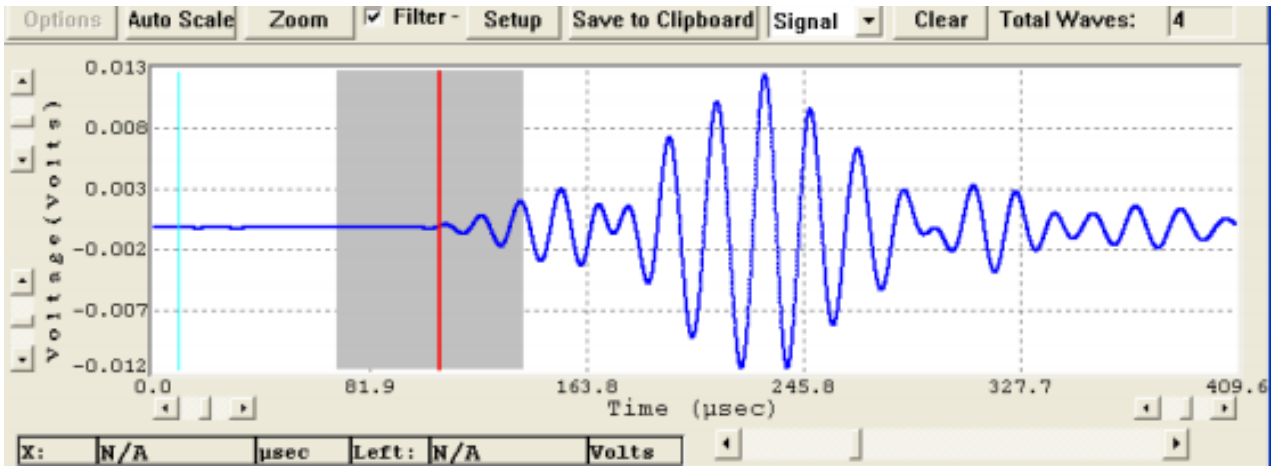

Figure 8. GCTS Ultrasonic Velocity Software voltage vs time graph.

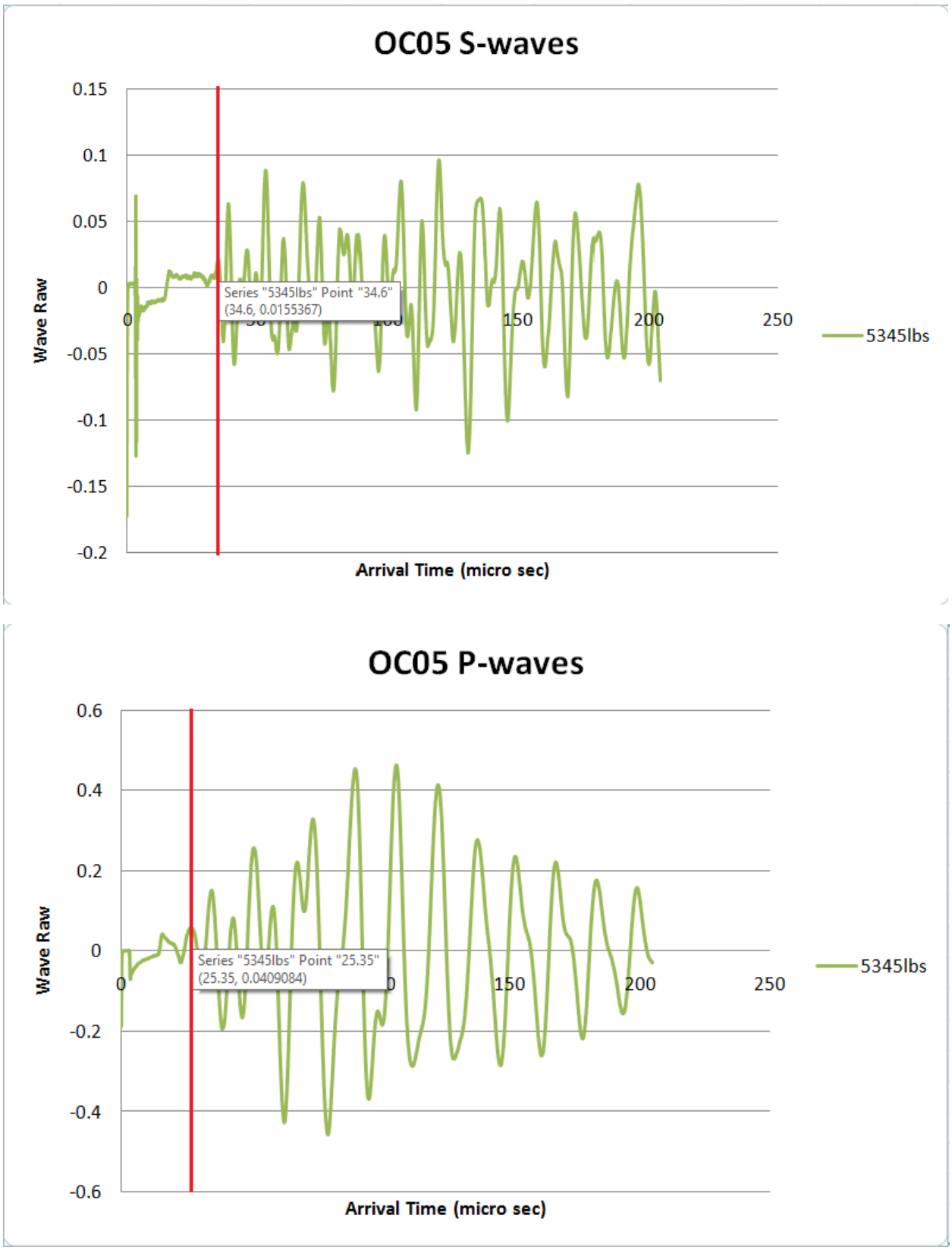

Figure 9. Example of P- and S-wave first arrival time picks from Excel.

				P(face to face) = 11.5	S (face to face) = 17.2
Sample	Vp(m/s)	Vs(m/s)	Specimen Heigh(m)	P arrival - (face to face)(sec)	S arrival - (face to face)(sec)
KC06	3114.19	1573.43	0.045	1.445E-05	2.860E-05
KC08	2909.09	1319.59	0.032	1.100E-05	2.425E-05
KC10	2810.81	1625.00	0.026	9.250E-06	1.600E-05
OC02	4404.76	1994.61	0.037	8.400E-06	1.855E-05
OC03	5333.33	2370.37	0.048	9.000E-06	2.025E-05
OC05	3317.54	1776.65	0.035	1.055E-05	1.970E-05
OC06	3466.04	1991.92	0.074	2.135E-05	3.715E-05
OC07	3076.92	1515.15	0.02	6.500E-06	1.320E-05
OC08	3459.46	1899.11	0.032	9.250E-06	1.685E-05
OC10	3237.41	1607.14	0.045	1.390E-05	2.800E-05
OC20	3844.16	2081.58	0.074	1.925E-05	3.555E-05
OC23	3250.00	1357.70	0.026	8.000E-06	1.915E-05
OC25	4459.46	2000.00	0.033	7.400E-06	1.650E-05

Table 2. Calculated first arrival times (baseline corrected) and subsequent P- and S-wave velocities.

Elastic parameters for each sample were determined using the calculated P- and S-wave velocities (Table 2). The acoustic impedance (Z) was determined by simply multiplying the P-wave velocity by the rock density ($Z=\rho V$). Young's Modulus (E) was calculated first by expressing the equation in terms of Vp and Vs as

$$E = \frac{\rho Vs^2(3Vp^2-4Vs^2)}{Vp^2-Vs^2} \qquad (1)$$

Young's Modulus (E) is a measure of the ratio of the uniaxial stress to uniaxial strain, or stiffness, of a material. This can be calculated by simply knowing the density (ρ) of the object, as well as, the compressional (Vp) and shear (Vs) velocities of the waveforms that traveled through the object. Poisson's Ratio was also calculated by expressing the equation in terms of Vp and Vs as

$$\nu = \frac{\left(\frac{Vp}{Vs}\right)^2-2}{2\left(\frac{Vp}{Vs}\right)^2-2} \qquad (2)$$

Poisson's Ratio (ν) is an elastic parameter that measures the ratio of transverse constructional strain to longitudinal extensional strain. More simply put it measures the degree to which a material expands outwards when squeezed, or contracts when stretched. Only the compression (Vp) and shear (Vs) waveform velocities need to be known to complete this calculation.

Lastly Lame's parameters of incompressibility (λ) and rigidity (μ) were calculated, using the previously determined Young's Modulus (E) and Poisson's Ratio (ν) numbers, with the following equations.

$$\lambda = \frac{E\nu}{(1+\nu)(1-2\nu)} \quad (3)$$

$$\square = \frac{E}{2(1+\nu)} \quad (4)$$

Mineral Brittleness

The mineralogical makeup of the cores has a large impact on brittleness and fracture potential. Rocks with an abundance of brittle minerals will have a higher brittleness index, and those with an abundance of ductile minerals will have a lower brittleness index. The mineral contents of the samples were calculated by combining XRF and XRD analyses of the cores by Janssen (2017). Several of the samples (KC06, KC10, KC08, OC06, OC23, OC05, and OC02) were also sent out to Stratochem Services for TOC and kerogen evaluation, whereas the rest of the samples had these data provided by Lambert (1993).

The process of evaluating brittleness index from mineralogical data was initially proposed by Jarvie et al. (2007) and Wang and Gale (2009) in the following equations:

$$BIJarvie = \frac{Qz}{Qz+Ca+Cly} \quad (5)$$

$$BIWang = \frac{Qz+Dol}{Qz+Ca+Dol+Cly+TOC} \quad (6)$$

where *Qz* is the weight % of quartz, *Ca* is the weight % of calcite, *Dol* is the weight % of dolomite, *Cly* is the weight % of clay, and *TOC* is the weight % of the total organic carbon (Xu and Sonnenberg, 2016).

My study used a variation of the equations shown above in order to take into account additional iron-rich minerals like pyrite, hematite, and iron oxides that are present in the Woodford shales. With these modifications, the new mineralogy BI equation is as follows:

$$BI = \frac{Qz+Dol+Pyr+FeTi}{Qz+Ca+Pyr+FeTi+Cly} \quad (7)$$

where *Qz* is the weight % of quartz, representing quartz, chert, and fossil tests. *Dol* is the weight % of dolostone present, *Pyr* is the weight % of pyrite present, and *FeTi* is the weight % of iron oxides present. *Cly* is represented by the weight %s of illite and chlorite added together.

To determine which minerals were present in the samples the whole-rock XRD data was used. Random powder mounts were analyzed, and the resulting 2θ and d-spacing of the peaks were measured and used to determine which minerals the peaks represented. An example of this can be seen in Figure 10, and the identification for the rest of the samples can be seen in Janssen (2017). With the knowledge of what minerals were present in the samples, the weight percentage of each mineral was calculated with the XRF data, assuming ideal mineral formulas.

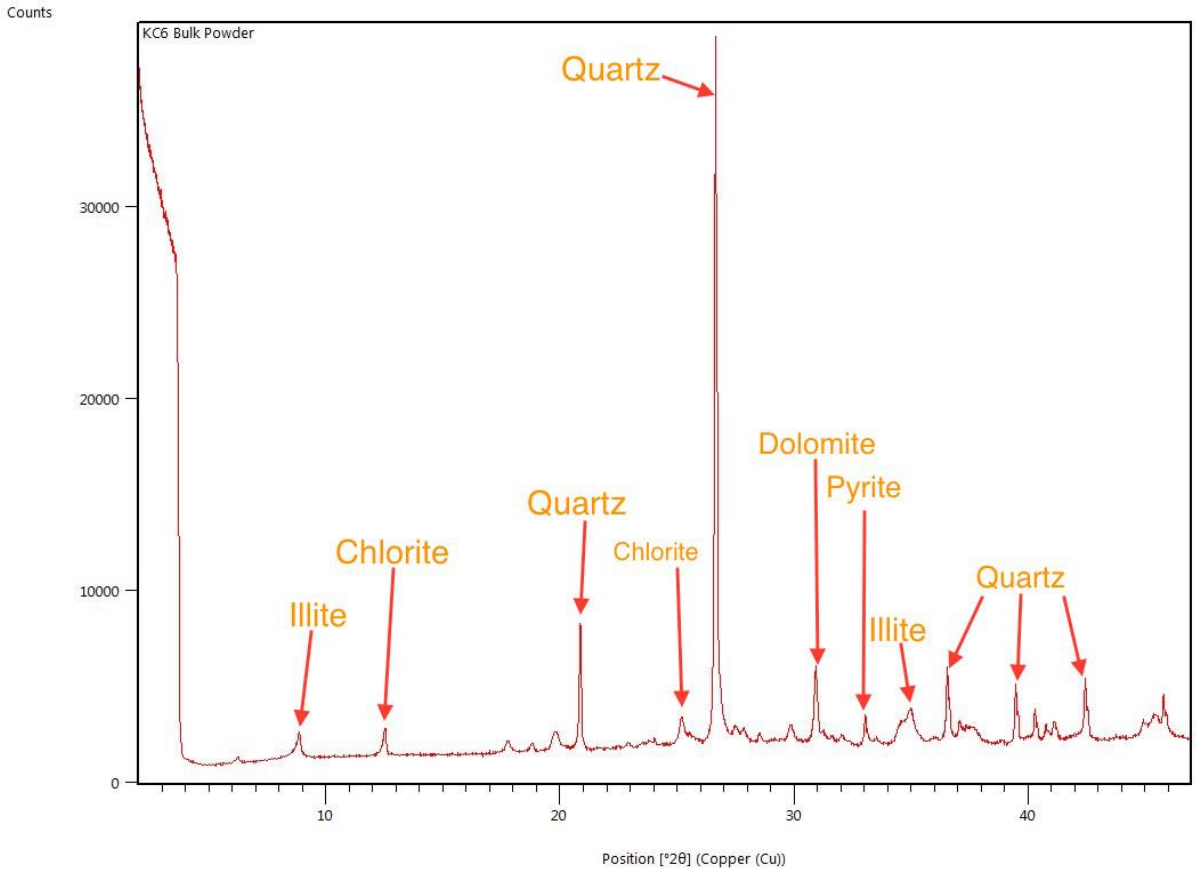

Figure 10. Mineral determinations from whole-rock XRD.

In order to calculate the mineralogy, the XRF major element data required some processing, and a few assumptions. The data was first converted from elemental weight percentage to a molar proportion by dividing the elemental weight percentage by the molar mass of the corresponding element. The elements V, Cr, and Mn, as well as Mg were ignored because they were only present in trace amounts, and because of detection problems using the HHXRF.

The newly calculated atomic atomic proportionswere used to calculate mineral weight percentages for each sample. The calculation involves allocating the elemental proportions of

each element to the mineralswith limiting elements first, then working toward the more complex minerals, keeping track of the remaining element proportions of each element not entirely used in the previous minerals. Calculations for this study began with the allotment of all of the S to pyrite (FeS_2) along with Fe in the amount of 1/2 of the alloted sufur.Next, Apatite ($Ca_5(PO_4)_3(OH,F,Cl)$) wascalculated, using all of the P.Hence the proportion of apatite is equal to $1/3^{rd}$ of theelemental proportion of P, using 5 times P of the Ca amount.The remaining Ca was alloted to dolomite ($(Ca,Mg)CO_3$). Iron oxides were then accounted for by alloting the entirity of Ti, along with an equal amount of Fe(assuming an ideal ilmenite ($FeTiO_3$)). At this point the remaining Fe was alloted to chlorite ($(Mg,Fe)_4Al_4Si_2O_{10}(OH)_8$).All of the K was attributed to illite, assuming a thermally mature illite (KAl2(Si,Al)4O10), which is actually closer to a muscovite. The remaining Si was calculated by subtracting the starting elemental proportions from the amount of Si alloted to illite and chlorite, and alloted to quartz (SiO_2). The molar proportions of each mineral was multiplied by that mineral's molar weight, resulting in mineral weights, which were summed together. Each mineral's weight was divided by the total,resulting in a weight percentage of each mineral.This process was repeated for all eleven samples to determine mineral weight percentages. With the use of equation 7 from above and the newly determined mineral weight percentages a mineralogically based brittleness index was calculated for each sample.A summary of the procedure is outlined in Table 3.

1. calc pyrite, apatite, Fe-Ti,illite using K, S, P, Ti
2. calculate excess Fe and Ca
3. put rest of Ca to dolomite
4. put rest of Fe to chlorite
5, calculate Si used in illite and chlorite
6. assign rest of Si to quartz

Table 3. Summary of procedure to calculate mineralogy from elemental data.

Limitations of Calculated Mineralogy

The methodology to calculate the mineral percentages in each sample involves several assumptions, and has limitastions. The only reason it is justified as the minerals calculated were identified independently by XRD. It should not be used without this intitial step. An adjustment to calculate a different mineralogy could be made in most cases.

Some of the underlying assumptions seem particularly valid, such as attributing all of the S to pyrite and all of then P to apatite. The rest become less confident. K could exist in a feldspar, although one would think that feldspar peaks would appear on XRD at fairly low concentrations because of its large structure factor. A bigger problem with illite is its highly variable chemistry. A simple formula that was almost a muscovite was used, but illites have been reported with variable K, Al, and Si based upon the phylosilicate formula of 10 O (Totten and Blatt, 1996). Table 4 illustrates this variability.

Smectite: Si^{+4}	K^+		Source
4.0	0.0	(ideal montmorillinite)	Ross and Hendricks (1945)
3.86	.06	(avg. of 6 mont.)	Deer et al. (1967)
3.96	—		Grim and Kulbicki (1961)
3.85	.08		Ramseyer and Boles (1986)
3.87	0.0	(avg. of 8 mont.)	Weaver (1989)
Illite:			
3.50	.75	(ideal illite)	Bailey (1984)
3.32	.57		Frey (1970)
3.39	.74	(avg of 4 $2M_1$ illites)	Weaver (1989)
3.40	.62		Weaver and Pollard (1973)
3.35	.65	(extrap. 100% illite)	Weaver (1989)
3.4	.6		Velde (1985)
3.42	.75		Warren and Curtis (1989)
Muscovite:			
3.0	1.0	(ideal muscovite)	Bailey (1984)
3.17	.78	(avg. 15 muscovites)	Deer et al. (1967)
3.09	.85		Rothbauer (1971)
3.02	.86		Güven (1971)
3.06	.93		Bailey (1984)

Table 4. Si^{+4} and K^+ concentrations of end-member physils (ions/10 oxygen) (Totten and Blatt, 1996).

Dolomite was calculated without using Mg, an obvious limitation. Mg is problematic with XRF, and HHXRF in particular, hence it was not considered. All of the Ca not in apatite was assigned to dolomite, because dolomite was first identified by XRD. Perhaps some of the Ca actually resides in expandable, smectite layers, as well as some Na, which also was not used in the calculations. This seems unlikely because expandable clays were not seen on glycolated XRD patterns, but remains a possibility. Chlorite was used in this study for the remaining clay, although the possibility that some was misidentified as kaolinite on XRD. Chlorite seemed reasonable because of the abundance of Fe, and previous reports of chlorite in the Woodford.

It should be noted that Al was not used in the mineral calculations, primarily because of its highly varied content in illite, which is a major mineral phase in the Woodford, both in the literature, and by XRD in this study. Attempts were made to include Al in the calculations, but were not successful. With these caveats in mind, the mineral calculations were judged more accurate than XRD by itself, and although undoubtedly not 100% accurate, should be a reasonable estimate for these very similar rocks, keeping in mind the limitations, and looking for relative variagtions.

Results

Elastic Parameters

The results of the rock density, Young's Modulus, Poisson's Ratio, Lamé's parameters of incompressibility (λ) and rigidity (μ), acoustic impedance, compression (Vp) and shear (Vs) wave velocity calculations can be seen in Table 5. The P- and S-wave velocities were calculated using the first arrival times measured using the ULT-100. The rest of the parameters, excluding

rock density, were determined using the calculated P- and S-wave velocities and the various equations mentioned in the methods section.

Sample	Vp(m/s)	Vs(m/s)	rho(density)g/cm3	Young's(Gpa)/10^6	Poisson's	Lame's Parameter (λ)	Lame's Parameter (μ)	Acoustic Impedance
KC06	3114.19	1573.43	2.13	14.03	0.33	10.13	5.28	6642.92
KC08	2909.09	1319.59	2.15	10.24	0.37	10.69	3.74	6242.38
KC10	2810.81	1460.67	2.15	12.04	0.32	7.79	4.58	6029.77
OC02	4404.76	1994.61	2.28	24.84	0.37	26.07	9.06	10031.50
OC03	5333.33	2370.37	2.20	34.03	0.38	37.85	12.36	11730.76
OC05	3317.54	1776.65	2.11	17.30	0.30	9.90	6.66	6997.09
OC06	3466.04	1991.92	2.35	23.34	0.25	9.57	9.31	8134.80
OC07	3076.92	1515.15	2.07	12.72	0.34	10.08	4.75	6363.77
OC08	3459.46	1899.11	2.12	19.67	0.28	10.10	7.66	7345.24
OC10	3237.41	1607.14	2.07	14.31	0.34	11.01	5.35	6708.87
OC20	3844.16	2081.58	2.13	23.81	0.29	12.99	9.21	8170.03
OC23	3250.00	1357.70	2.06	10.58	0.39	14.15	3.79	6689.11
OC25	4459.46	2000.00	2.53	27.86	0.37	30.12	10.14	11300.82

Table 5. Calculated elastic parameters for the 13 Woodford core samples.

In addition to the calculated elastic parameters information on TOC weight percentage, Tmax (temp. at which maximum rate of hydrocarbon generation happens), and kerogen type are provided by Lambert (1993) and the Stratochem Services laboratory (Table 6).

Sample	Tmax	% TOC	Kerogen Type
KC06	440	2.2	2
KC08	441	4.3	1.5
KC10	439	0.5	3
OC02	442	1.2	2
OC03	446	5.3	1.5
OC05	447	6.8	1.5
OC06	445	4.4	1.5
OC07	446	5.2	1
OC08	486	4.1	4
OC10		12.7	
OC20	430	0.4	immature
OC23		7.0	1
OC25	445	7.8	1

Table 6. TOC weight percentage, Tmax, and kerogen type values for the 13 Woodford cores, provided by Lambert (1993) (KC06, KC08, KC10, OC02-08) and Stratochem Services (KC06, KC08, KC10, OC02, OC05, OC06, and OC23).

Mineral Analysis

The XRF analysis on the cores was done by Kale Janssen (2017) in conjunction with this study. Both major and trace elements were measured, but only the major elements were used in this study. The results of the XRF analysis for the major elements can be seen in Table 7. The mineralogy calculations and resulting mineral weight percentages can be seen in Tables 8-10, and the calculated mineralogy for all eleven samples can be seen in table 11.

Sample	AlKa1	SiKa1	P Ka1	S Ka1	K Ka1	CaKa1	TiKa1	V Ka1	CrKa1	MnKa1	FeKa1
KC06	6.46	20.58	0.03	0.98	3.67	1.67	0.43	0.01	0.01	0.03	3.81
KC08	6.17	16.22	0.03	1.04	4.54	0.84	0.44	0.02	0.01	0.03	3.79
KC10	6.42	16.52	0.03	0.76	4.15	0.98	0.45	0.01	0.01	0.03	4.24
OC02	1.43	20.50	0.06	0.36	0.95	6.82	0.15	0.01	0.01	0.03	0.89
OC03	2.89	31.34	0.04	0.85	1.45	0.34	0.21	0.06	0.01	0.03	1.15
OC05	3.21	24.48	0.04	0.46	2.59	0.23	0.28	0.09	0.01	0.02	1.34
OC06	5.14	15.54	0.03	1.43	3.90	3.66	0.36	0.01	0.01	0.04	3.94
OC07	4.41	20.11	0.02	0.97	3.01	0.39	0.32	0.03	0.01	0.02	3.22
OC08	4.93	17.31	0.02	1.90	3.82	3.31	0.37	0.04	0.01	0.03	2.96
OC20	3.48	31.36	0.05	0.85	1.60	0.44	0.23	0.03	0.02	0.03	1.32
OC25	5.19	22.28	0.12	4.66	2.95	0.22	0.31	0.02	0.01	0.02	6.16

Table 7. XRF major element weight percentages for 11 of the 13 Woodford core samples.

KC06				
mineral	Ele. Prop.	mineral ml. mass	mineral wt.	mineral wt. %
illite(KAl2(Si,Al)4O10)	7.72	389.00	3002.22	45.78
pyrite(FeS2)	1.25	119.98	150.51	2.30
apatite(Ca5(PO4)3(OH,F,Cl))	0.03	509.00	12.83	0.20
fe-ti oxides(FeTiO3)	0.73	151.70	111.14	1.69
dolomite((Ca,Mg) CO3)	3.36	184.40	618.89	9.44
chlorite((Mg, Fe)4Al4Si2O10(OH)8)	0.91	595.00	540.20	8.24
quartz(SiO2)	35.31	60.08	2121.59	32.35
		total	6557.38	
KC08				
mineral	Ele. Prop.	mineral ml. mass	mineral wt.	mineral wt. %
illite(KAl2(Si,Al)4O10)	11.01	389.00	4283.21	63.34
pyrite(FeS2)	1.54	119.98	185.25	2.74
apatite(Ca5(PO4)3(OH,F,Cl))	0.03	509.00	14.35	0.21
fe-ti oxides(FeTiO3)	0.88	151.70	133.40	1.97
dolomite((Ca,Mg) CO3)	1.94	184.40	358.43	5.30
chlorite((Mg, Fe)4Al4Si2O10(OH)8)	1.00	595.00	597.72	8.84
quartz(SiO2)	19.80	60.08	1189.70	17.59
		total	6762.04	
KC10				
mineral	Ele. Prop.	mineral ml. mass	mineral wt.	mineral wt. %
illite(KAl2(Si,Al)4O10)	9.95	389.00	3871.81	57.78
pyrite(FeS2)	1.11	119.98	132.65	1.98
apatite(Ca5(PO4)3(OH,F,Cl))	0.03	509.00	17.18	0.26
fe-ti oxides(FeTiO3)	0.87	151.70	132.59	1.98
dolomite((Ca,Mg) CO3)	2.25	184.40	414.57	6.19
chlorite((Mg, Fe)4Al4Si2O10(OH)8)	1.29	595.00	765.14	11.42
quartz(SiO2)	22.75	60.08	1366.80	20.40
		total	6700.74	
OC02				
mineral	Ele. Prop.	mineral ml. mass	mineral wt.	mineral wt. %
illite(KAl2(Si,Al)4O10)	2.40	389.00	935.15	11.47
pyrite(FeS2)	0.56	119.98	67.20	0.82
apatite(Ca5(PO4)3(OH,F,Cl))	0.07	509.00	33.97	0.42
fe-ti oxides(FeTiO3)	0.32	151.70	48.30	0.59
dolomite((Ca,Mg) CO3)	16.59	184.40	3058.98	37.53
chlorite((Mg, Fe)4Al4Si2O10(OH)8)	0.18	595.00	104.48	1.28
quartz(SiO2)	64.95	60.08	3902.36	47.88
		total	8150.45	

Table 8. Mineral weight percentage calculations for samples KC06, KC08, KC10, and OC02.

OC03				
mineral	Ele. Prop.	mineral ml. mass	mineral wt.	mineral wt. %
illite(KAl2(Si,Al)4O10)	2.80	389.00	1088.17	18.17
pyrite(FeS2)	1.00	119.98	120.09	2.00
apatite(Ca5(PO4)3(OH,F,Cl))	0.04	509.00	18.36	0.31
fe-ti oxides(FeTiO3)	0.33	151.70	49.74	0.83
dolomite((Ca,Mg) CO3)	0.62	184.40	114.26	1.91
chlorite((Mg, Fe)4Al4Si2O10(OH)8)	0.06	595.00	35.15	0.59
quartz(SiO2)	75.96	60.08	4563.81	76.20
		total	**5989.58**	
OC05				
mineral	atomic wt. %	mineral ml. mass	mineral wt.	mineral wt. %
illite(KAl2(Si,Al)4O10)	5.99	389.00	2328.43	36.60
pyrite(FeS2)	0.65	119.98	77.47	1.22
apatite(Ca5(PO4)3(OH,F,Cl))	0.04	509.00	20.19	0.32
fe-ti oxides(FeTiO3)	0.52	151.70	79.57	1.25
dolomite((Ca,Mg) CO3)	0.49	184.40	91.14	1.43
chlorite((Mg, Fe)4Al4Si2O10(OH)8)	0.25	595.00	147.09	2.31
quartz(SiO2)	60.21	60.08	3617.68	56.87
		total	**6361.56**	
OC06				
mineral	Ele. Prop.	mineral ml. mass	mineral wt.	mineral wt. %
illite(KAl2(Si,Al)4O10)	9.45	389.00	3675.43	48.91
pyrite(FeS2)	2.11	119.98	252.63	3.36
apatite(Ca5(PO4)3(OH,F,Cl))	0.03	509.00	13.55	0.18
fe-ti oxides(FeTiO3)	0.71	151.70	108.36	1.44
dolomite((Ca,Mg) CO3)	8.47	184.40	1562.60	20.79
chlorite((Mg, Fe)4Al4Si2O10(OH)8)	0.96	595.00	573.97	7.64
quartz(SiO2)	22.10	60.08	1327.82	17.67
		total	**7514.35**	
OC07				
mineral	atomic wt. %	mineral ml. mass	mineral wt.	mineral wt. %
illite(KAl2(Si,Al)4O10)	7.25	389.00	2819.84	43.98
pyrite(FeS2)	1.42	119.98	170.78	2.66
apatite(Ca5(PO4)3(OH,F,Cl))	0.02	509.00	10.96	0.17
fe-ti oxides(FeTiO3)	0.64	151.70	96.62	1.51
dolomite((Ca,Mg) CO3)	0.91	184.40	167.13	2.61
chlorite((Mg, Fe)4Al4Si2O10(OH)8)	0.84	595.00	501.32	7.82
quartz(SiO2)	44.04	60.08	2645.67	41.26
		total	**6412.31**	

Table 9. Mineral weight percentage calculations for samples OC03-07.

OC08				
mineral	Ele. Prop.	mineral ml. mass	mineral wt.	mineral wt. %
illite(KAl2(Si,Al)4O10)	8.89	389.00	3458.52	48.06
pyrite(FeS2)	2.70	119.98	324.37	4.51
apatite(Ca5(PO4)3(OH,F,Cl))	0.02	509.00	8.05	0.11
fe-ti oxides(FeTiO3)	0.70	151.70	106.41	1.48
dolomite((Ca,Mg) CO3)	7.38	184.40	1361.70	18.92
chlorite((Mg, Fe)4Al4Si2O10(OH)8)	0.36	595.00	212.00	2.95
quartz(SiO2)	28.71	60.08	1725.03	23.97
		total	7196.08	
OC20				
mineral	atomic wt. %	mineral ml. mass	mineral wt.	mineral wt. %
illite(KAl2(Si,Al)4O10)	3.02	389.00	1174.65	19.67
pyrite(FeS2)	0.97	119.98	116.80	1.96
apatite(Ca5(PO4)3(OH,F,Cl))	0.04	509.00	20.81	0.35
fe-ti oxides(FeTiO3)	0.36	151.70	54.24	0.91
dolomite((Ca,Mg) CO3)	0.78	184.40	143.76	2.41
chlorite((Mg, Fe)4Al4Si2O10(OH)8)	0.10	595.00	61.78	1.03
quartz(SiO2)	73.22	60.08	4398.77	73.67
		total	5970.82	
OC25				
mineral	Ele. Prop.	mineral ml. mass	mineral wt.	mineral wt. %
illite(KAl2(Si,Al)4O10)	5.66	389.00	2202.62	37.41
pyrite(FeS2)	5.45	119.98	653.88	11.11
apatite(Ca5(PO4)3(OH,F,Cl))	0.10	509.00	50.32	0.85
fe-ti oxides(FeTiO3)	0.48	151.70	73.10	1.24
dolomite((Ca,Mg) CO3)	0.39	184.40	72.57	1.23
chlorite((Mg, Fe)4Al4Si2O10(OH)8)	0.59	595.00	348.21	5.91
quartz(SiO2)	41.38	60.08	2486.39	42.23
		total	5887.10	

Table 10. Mineral weight percentage calculations for samples OC08, OC20, and OC25.

			Wt % of calculated mineralogy					
Sample	illite	pyrite	FeTi oxides	apatite	chlorite	dolomite	qtz/chert/fossil tests	Mineral BI
KC06	45.78	2.30	1.69	0.20	8.24	9.44	32.35	45.87
KC08	63.34	2.74	1.97	0.21	8.84	5.30	17.59	27.67
KC10	57.78	1.98	1.98	0.26	11.42	6.19	20.40	30.62
OC02	11.47	0.82	0.59	0.42	1.28	37.53	47.88	55.65
OC03	18.17	2.00	0.83	0.31	0.59	1.91	76.20	81.19
OC05	36.60	1.22	1.25	0.32	2.31	1.43	56.87	60.96
OC06	48.91	3.36	1.44	0.18	7.64	20.79	17.67	43.35
OC07	43.98	2.66	1.51	0.17	7.82	2.61	41.26	48.12
OC08	48.06	4.51	1.48	0.11	2.95	18.92	23.97	48.94
OC20	19.67	1.96	0.91	0.35	1.03	2.41	73.67	79.22
OC25	37.41	11.11	1.24	0.85	5.91	1.23	42.23	56.30

Table 11. Calculated mineralogy and mineral-based brittleness index of all 11 samples.

Discussion

Elastic Brittleness Index

With laboratory measurements of compression and shear wave velocities taken for each core, a variety of elastic parameters are available for evaluation. One of the first definitions, predominant in geophysical literature, states that rocks characterized by a high brittleness index exhibit a high Young's modulus (E) and low Poisson's ratio (ν) (Herwanger et al., 2015). On the other hand, Goodway et al. (2007) related E and ν to the more intuitive Lamé parameters of incompressibility λ and rigidity μ through the following relationships

$$E = \frac{\square(3\lambda+2\square)}{\lambda+\square} \quad (8)$$

$$\nu = \frac{\lambda}{2(\lambda+\square)} \quad (9)$$

and found that the increase in μ leads to an increase in E and a decrease in ν. Therefore, μ may represent a good indicator of brittleness index (Guo et al., 2013). Lamé's parameter of rigidity was chosen to represent the elastic BI in this study due to its better correlation with E/ν ratios (Fig. 11) and Goodway's evaluation of the parameters.

Due to the samples being run under1/5 of their *in situ* questions arose regarding the impact of overburden pressure on elastic parameter calculations. The shales currently present in the basin would be under much higher overburden pressures resulting in much faster P- and S-wave velocities, but the relationship between Vp and Vs should remain linear. Jaiswal et. al (2014) found that Vp and Vs maintain a linear relationship with increasing effective pressures (Fig. 12) and this can be confirmed in this study using sample KC10 as an example (Fig. 13).

With this evidence of a linear trend between Vp and Vs with increasing overburden pressures it can be concluded that increasing pressure will have little to no impact on the calculation of elastic parameters.

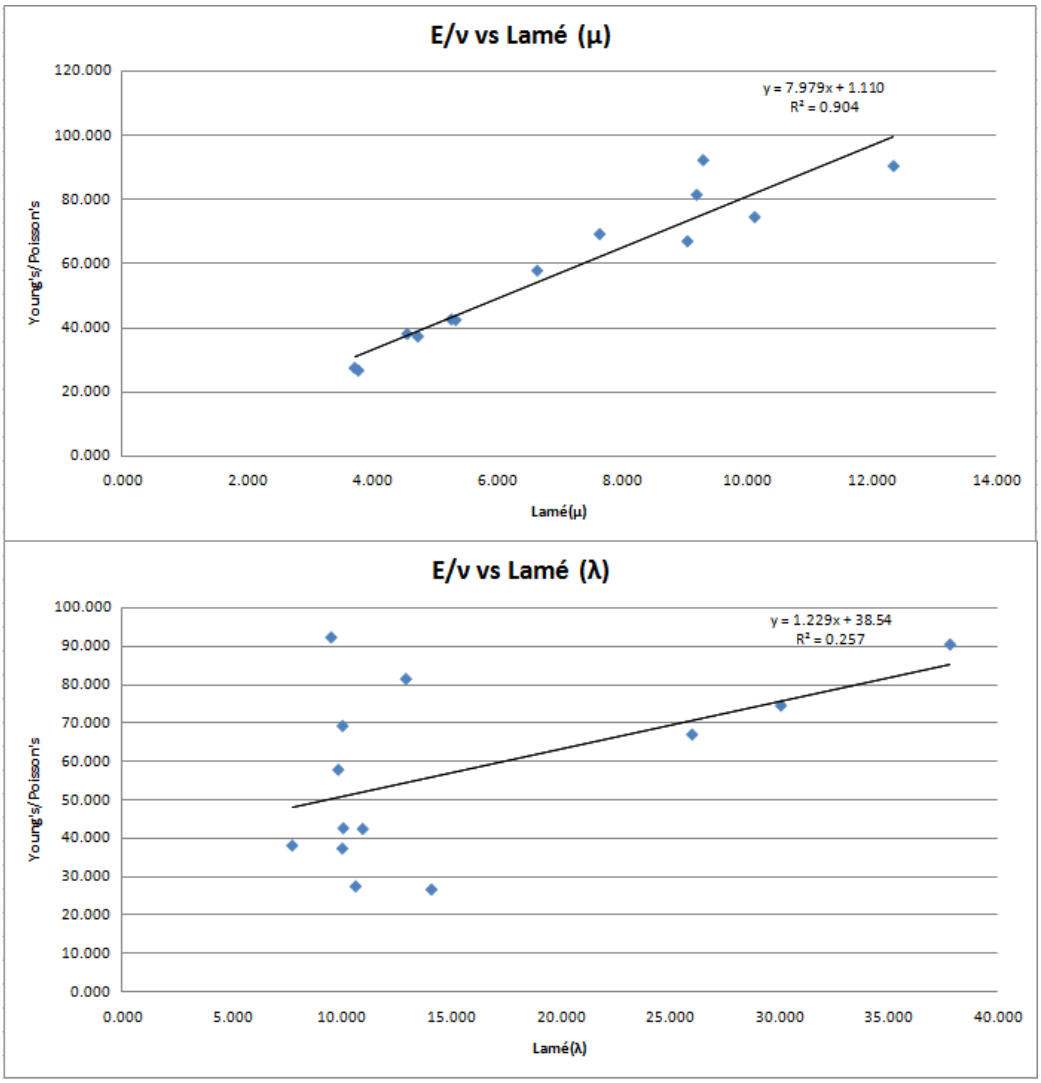

Figure 11. Lamé parameters (μ) and (λ) vs E/ν depicting that rigidity (μ) has a better fit.

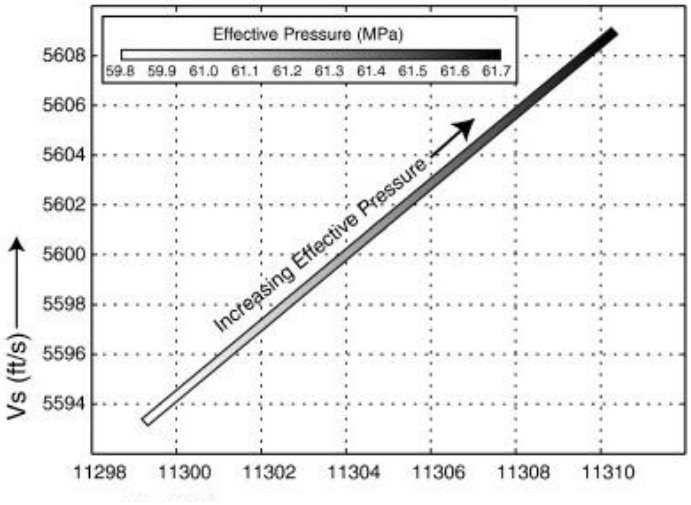

Figure 12. Graph depicting linear correlation between Vp and Vs with increasing effective pressure (Jaiswal et al. (2014)).

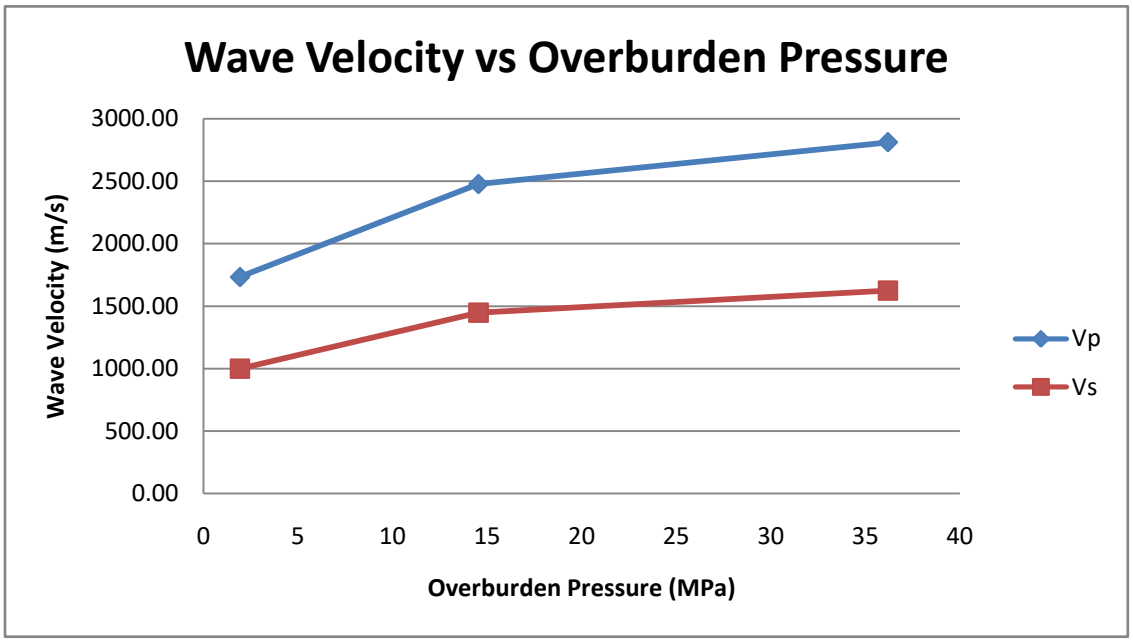

Figure 13. Graph of sample KC10 under three different pressures. A linear correlation between Vp and Vs is observed with increasing overburden pressure.

The elastic brittleness index, represented by Lamé (μ), was correlated with a variety of physical and mineral rock properties in an attempt to evaluate which specific rock properties have an effect on brittleness index. Previous studies done by Wang and Gale (2009) found that

TOC increases the ductility of the rocks, while other studies like that of Altamar and Marfurt (2014) found that TOC does not have a significant impact on ductility. This study has shown that TOC has no correlation with the elastic brittleness index due to its wide spread variation (Fig. 14). This may have been due to the limited sample size, but other studies have made the same observation.

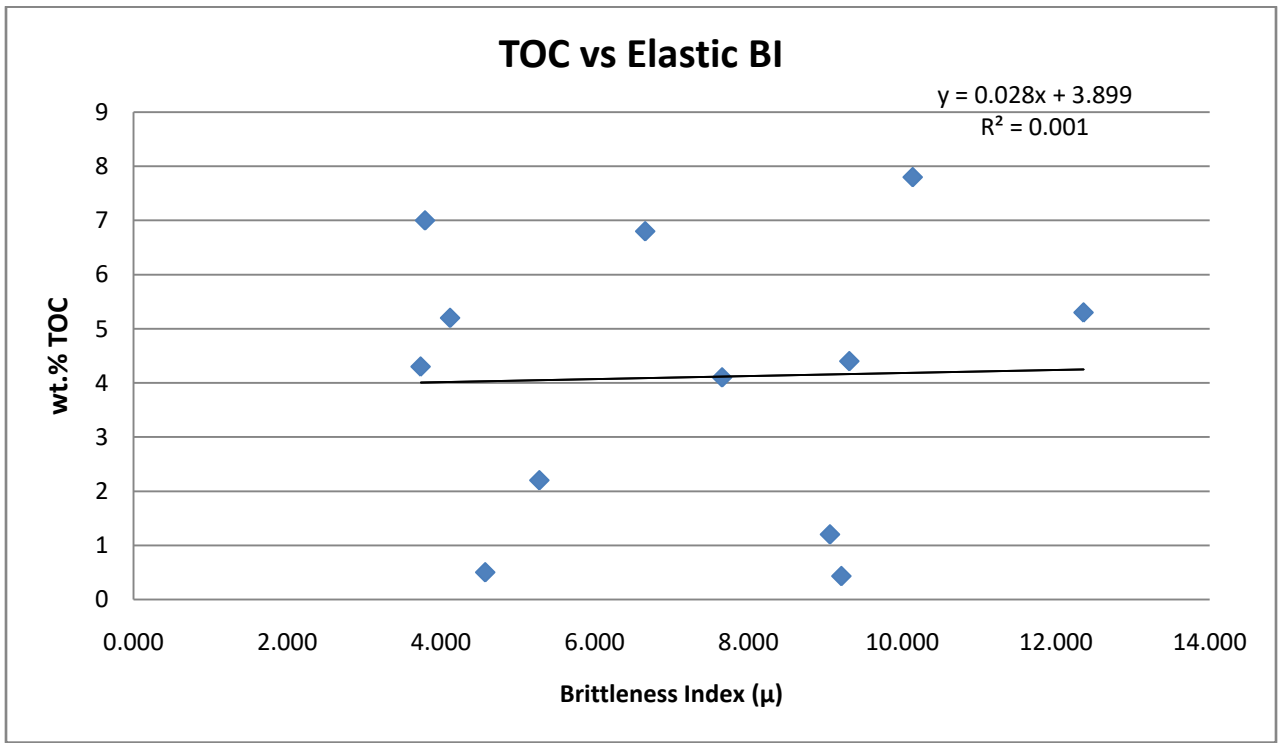

Figure 14. Graph depicting lack of correlation between TOC and elastic BI .

A strong correlation between acoustic impedance and elastic brittleness index (BI) indicates mineralogical variation within the shales is properly accounted for (Fig. 15). With this confirmation the elastic BI of each sample was correlated with the calculated mineral weight percentages. Sample OC02 was considered an outlier and removed from the data during correlations due to its mineralogical makeup not being consistent with a shale and more like a

micrite as seen in Table 6. With OC02 removed the correlations were much more representative of the date being evaluated (Fig. 16).

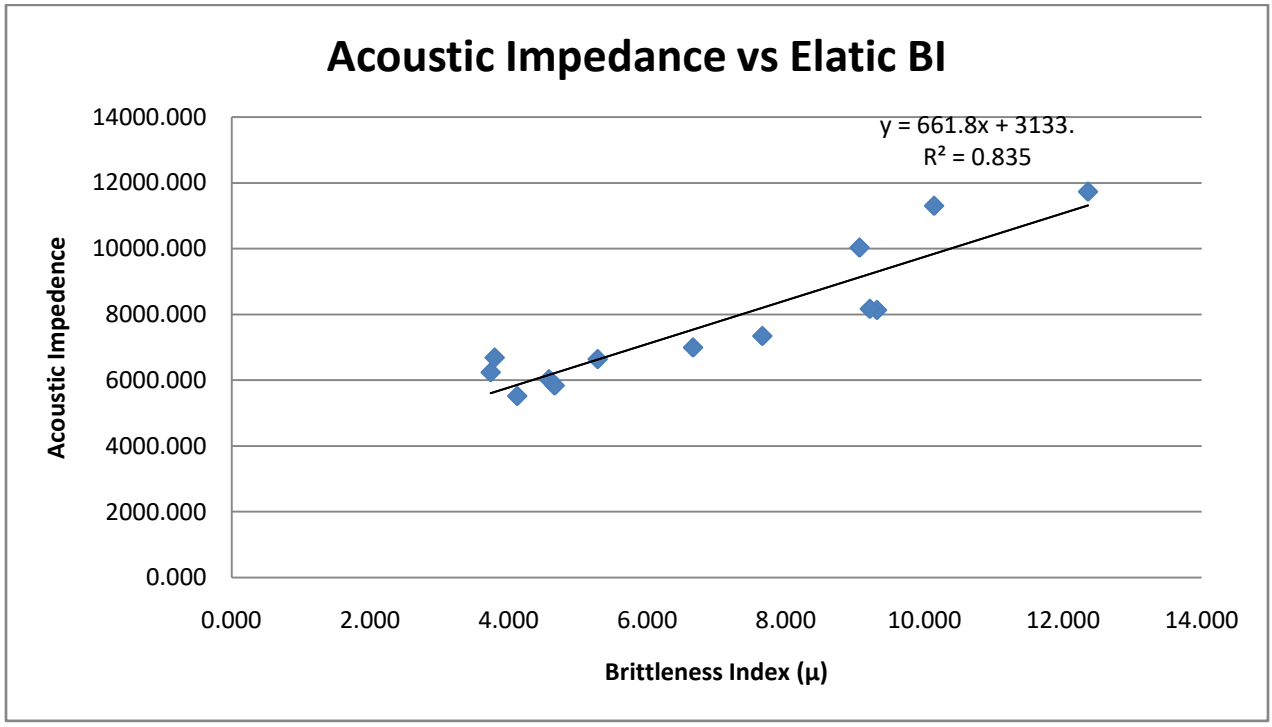

Figure 15. Graphs depicting correlation of acoustic impedance with elastic brittleness.

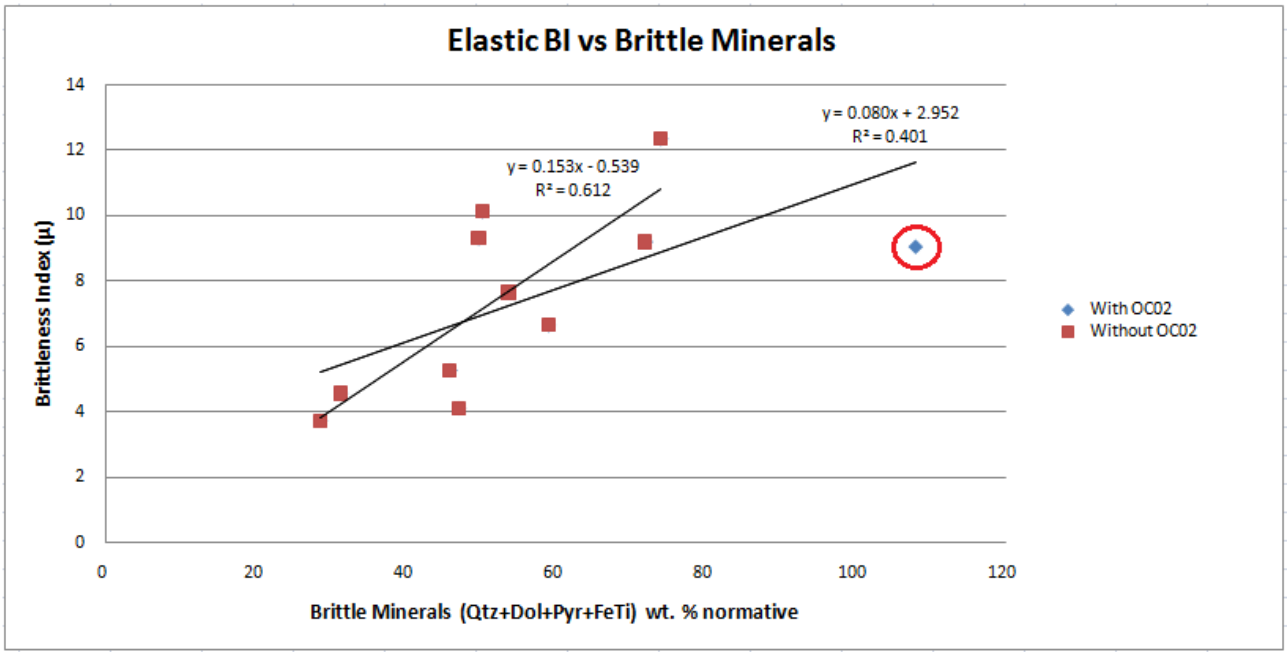

Figure 16. Graphs depicting correlations with OC02 present and without. Sample OC02 is circle in red.

A positive correlation between elastic BI and quartz was observed. While carbonate concentrations on their own appear to have no impact on brittleness. This may be due to the variability in the fabric makeup of dolostones. When compared to all of the brittle minerals (Qtz, Dol, Pyr, and FeTi) there is a reasonably strong positive correlation present. On the other hand clays minerals, like illite and chlorite, have shown a strong negative correlation with brittleness.

For the Middle Woodford Member cores evaluated, an increase of clay content causes the reduction of elastic brittleness, while higher quartz, carbonate, pyrite, and FeTi oxides concentrations contribute to an increase in elastic brittleness (Fig. 17). This evaluation may not be accurate for all of the Woodford shale members. The lack of available samples from other shale members, during the time of this study, prevented investigation into brittleness variation between shale members. Correlations with Tmax and vitrinite reflectance were unable to be

performed due to the lack in variation of these data across the samples. A possible cause of this could be the fact that a majority of the 13 samples are all from the middle shale member.

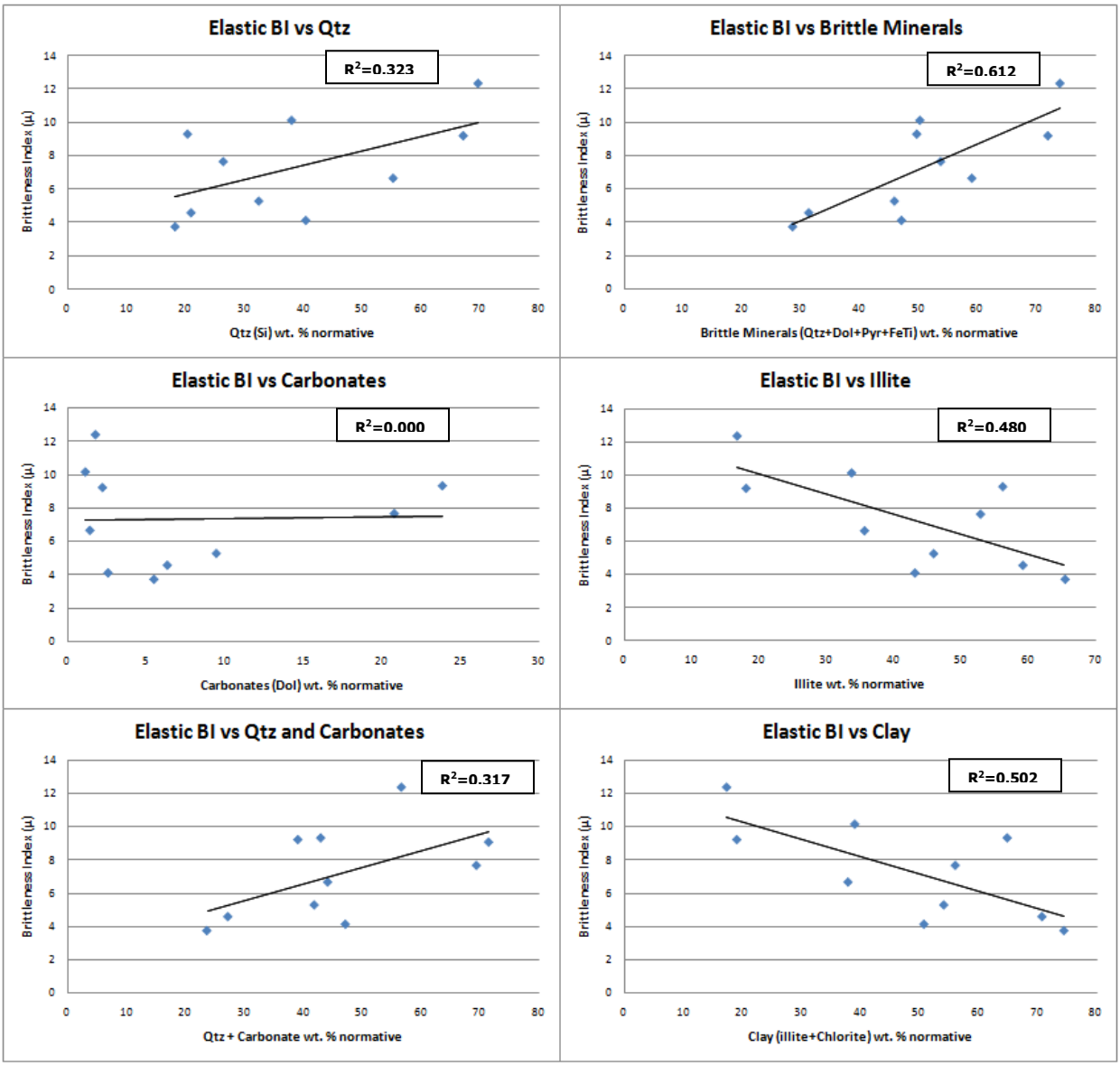

Figure 17. Impact of calculated mineral weight percentages on the elastic BI of the Woodford shale.

Mineral Brittleness Index

The Woodford Formation appears to be composed of six major minerals quartz, dolostone, pyrite, FeTi oxides, illite, and chlorite with minor amounts of apatite present. The Woodford portion of the Anadarko Basin has, in general, a siliceous mudstone present throughout. The minerals quartz, dolostone, pyrite, and FeTi oxides are considered to be brittle minerals and clay minerals illite and chlorite are considered to be ductile for the middle shale member of the Woodford Formation. As seen with elastic BI, there are again no indications that TOC has any effect on mineral BI in this study (Fig.18). This may be due to the small sample size limiting the range of TOC values for evaluation. With a much larger sample size a correlation with TOC may be observed, but there is no correlation seen in this study. Due to this lack of correlation TOC was no used in the calculation of mineral BI.

While calculating the mineral weight percentages, as mention in the methods section, there was an excess of aluminum observed. With aluminum being present in so many states, like unaxial, biaxial, and triaxial, determining its proper allocation was not possible. This results in a small level of uncertainty in the mineral weight percentage calculations. The calculated mineral weight percentages were incorporated into the previously expressed equations by Jarvie et al (2007) and Wang and Gale (2009) to produce a new mineralogy based brittleness index for the Woodford (equation 7). The calculated mineral BI was correlated with the various mineral weight percentages. As seen before with elastic BI quartz shows a strong positive correlation with mineral BI. Carbonates on their own show little correlation. In the case of mineral BI when the carbonates are combined with quartz the correlation becomes only slightly better. This may be due to the fabric of the dolostone and the stress placed on it. When compared to all of the brittle minerals together mineral BI predictably shows a strong positive correlation (Fig. 19).

Unsurprisingly the mineral BI correlates with the calculated mineral weight percentages better than the elastic BI, due to it being defined from the minerals weights. The ductile clay minerals illite and chlorite show a very strong negative correlation with the mineral BI (Fig. 19).

The mineral BI once again shows that the middle shale member of the Woodford Formation is made more ductile with the presence of clays like illite and chlorite, whereas the brittle minerals quartz, carbonates, FeTi oxides, and pyrite contribute to an increase in the brittleness index (Fig. 19). This indicates a good correlation between the elastic BI and the mineral BI, which can be seen in Figure 20.

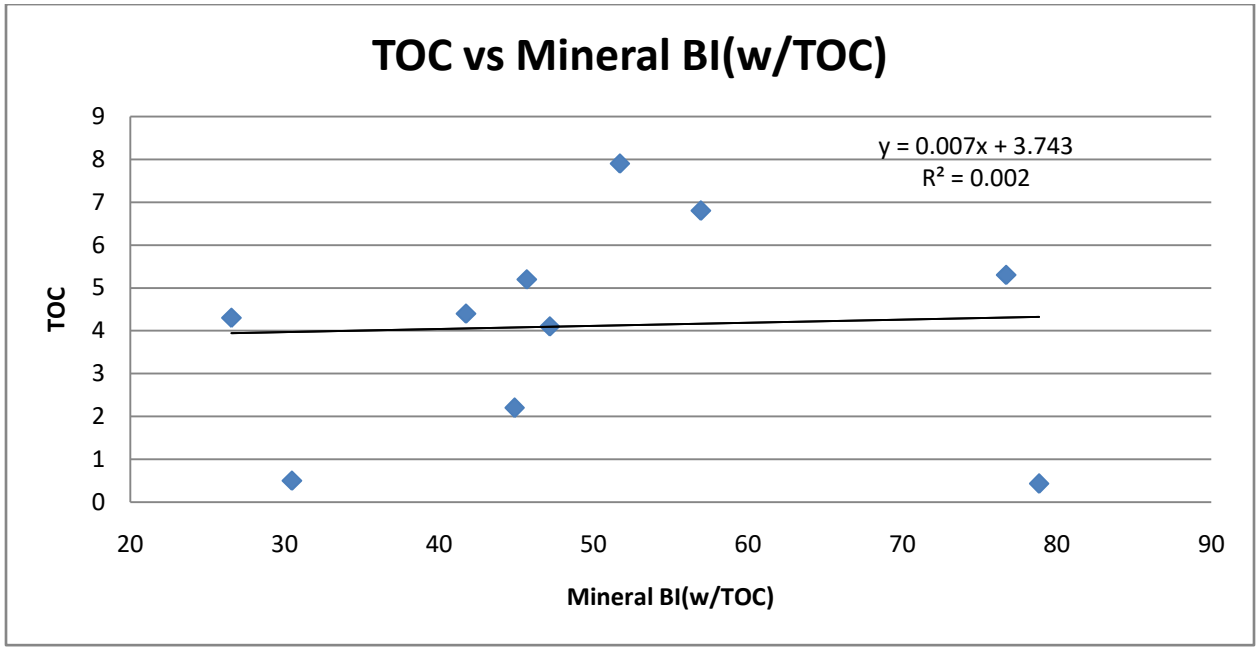

Figure 18. Graph of TOC vs mineral BI calculated with TOC. No correlation between TOC and mineral BI is seen.

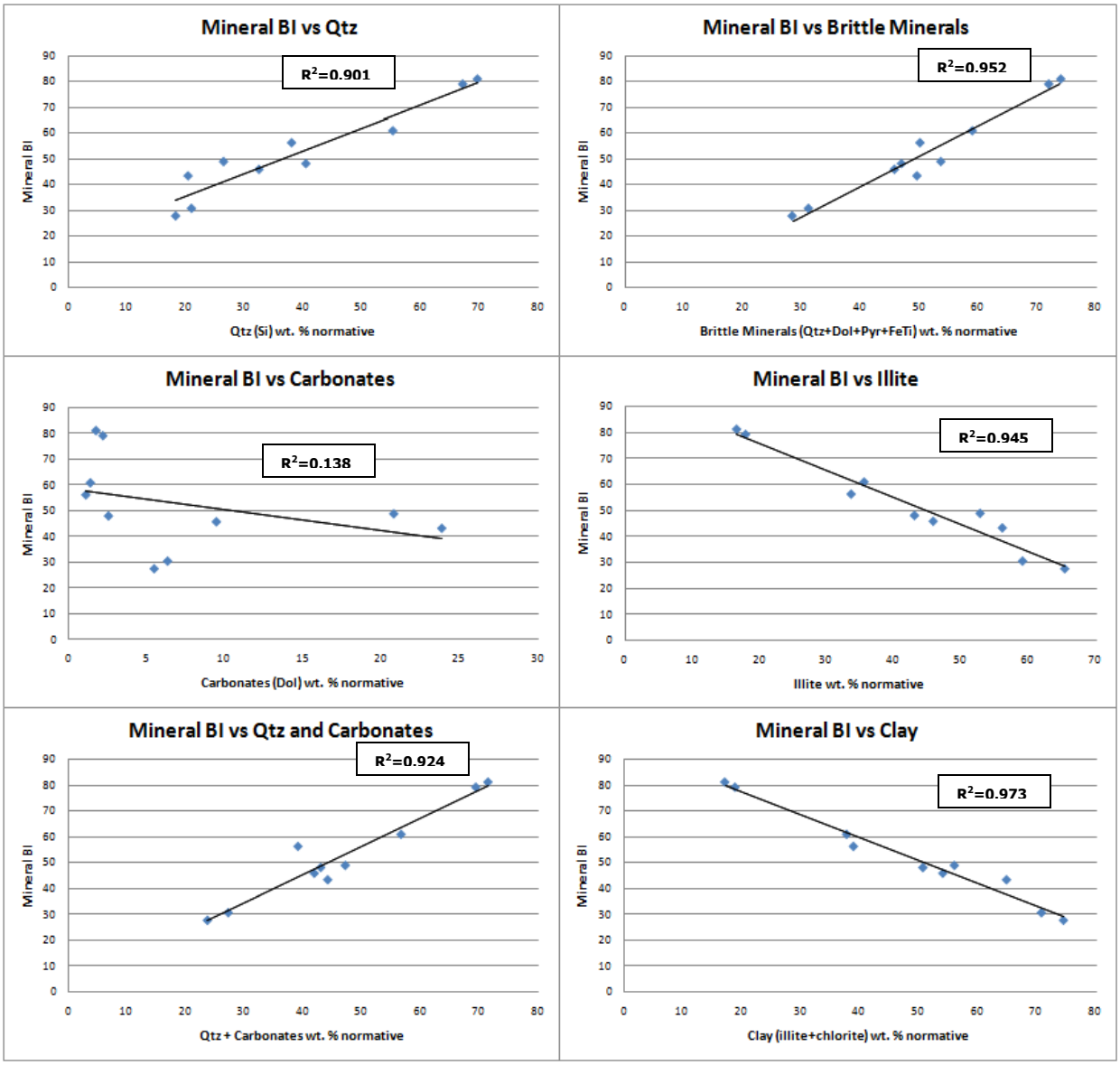

Figure 19. Impact of calculated mineral weight percentages on the mineral BI of the Woodford shale.

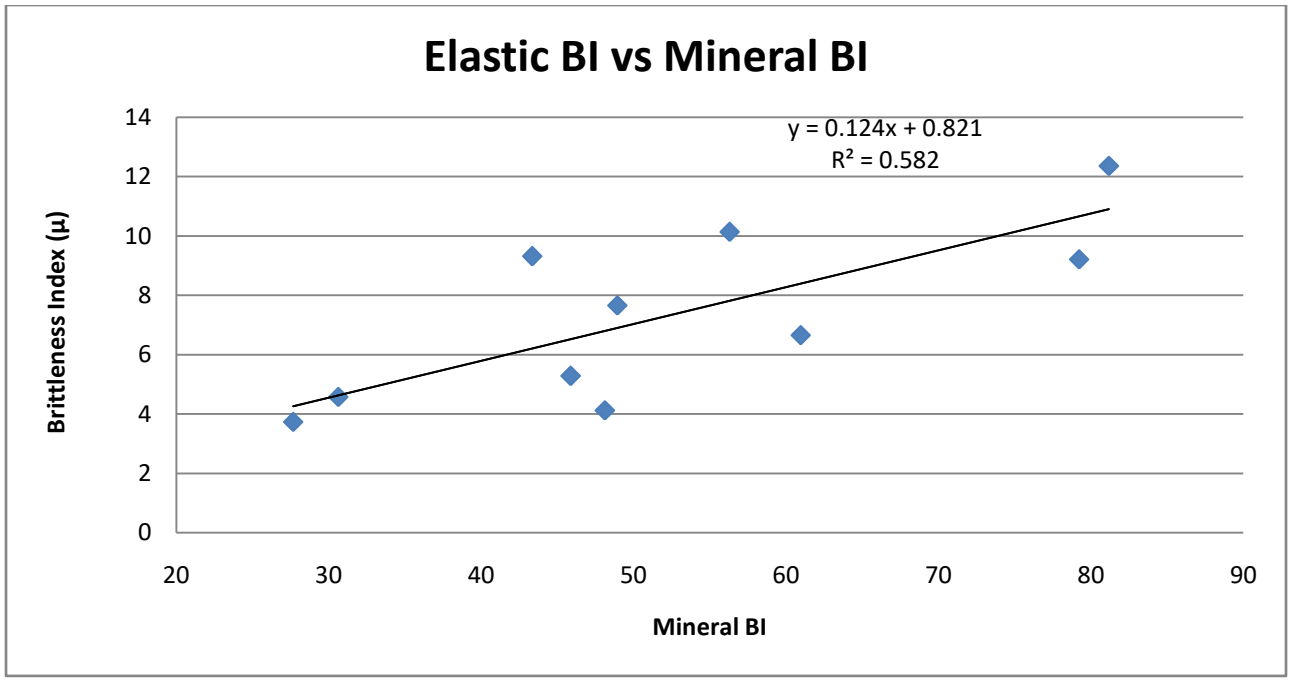

Figure 20. Graph depicting the correlation between the elastic BI and mineral BI.

Figure 20 demonstrates the correlation between all three mineralogy-based BI results, as well as, their correlations with Young's Modulus, Poisson's Ratio, acoustic impedance, elemental BI, and the elastic BI. Mineral BIs were calculated for both the Gale and Wang (2009) and Jarvie et al. (2007) mineral brittleness index methods (equation 5 and 6) using the calculated mineral weight percentages from this study. An elemental BI was calculated for comparison by taking the elements most commonly found in brittle minerals like Si, Ca, and Fe, and dividing them by elements found in ductile minerals like K and Al. The Wang and Gale (2009) method shows an underestimation of the brittleness index due to the absence of pyrite and hematite as brittle minerals. The Jarvie et al (2007) method also shows an occasional underestimation of brittleness due to the absence of pyrite and hematite. The basic elemental BI calculation shows a blanket overestimation of brittleness due to no Si being allocated to the ductile minerals. If a correlation

factor between mineral BI and elemental BI can be worked out in future studies, elemental BI could be a reasonable method for predicting brittleness.

The method used in this study correlates well with elastic BI to start, but appears to be much flatter than the elastic BI after the first peak. This may be due to a lack of mineralogical variation through that set of samples. This may indicate that there is another major factor at play in the elastic BI that was unable to be evaluated in this study. The elemental BI shows similar tracking with a blanket overestimation of brittleness (Figs. 21-22). The elastic based BI used for this study shows a good correlation with other elastic properties, as well as, the mineralogical based BI. All of the geomechanical parameters are in a general agreement on brittleness estimations. Zones with a higher elastic BI are confirmed by the presence of a higher Young's Modulus, higher acoustic impedance, and higher mineral BI. Poisson's Ratio shows slightly more variation due to the mineralogical differences in the core samples (Fig. 21).

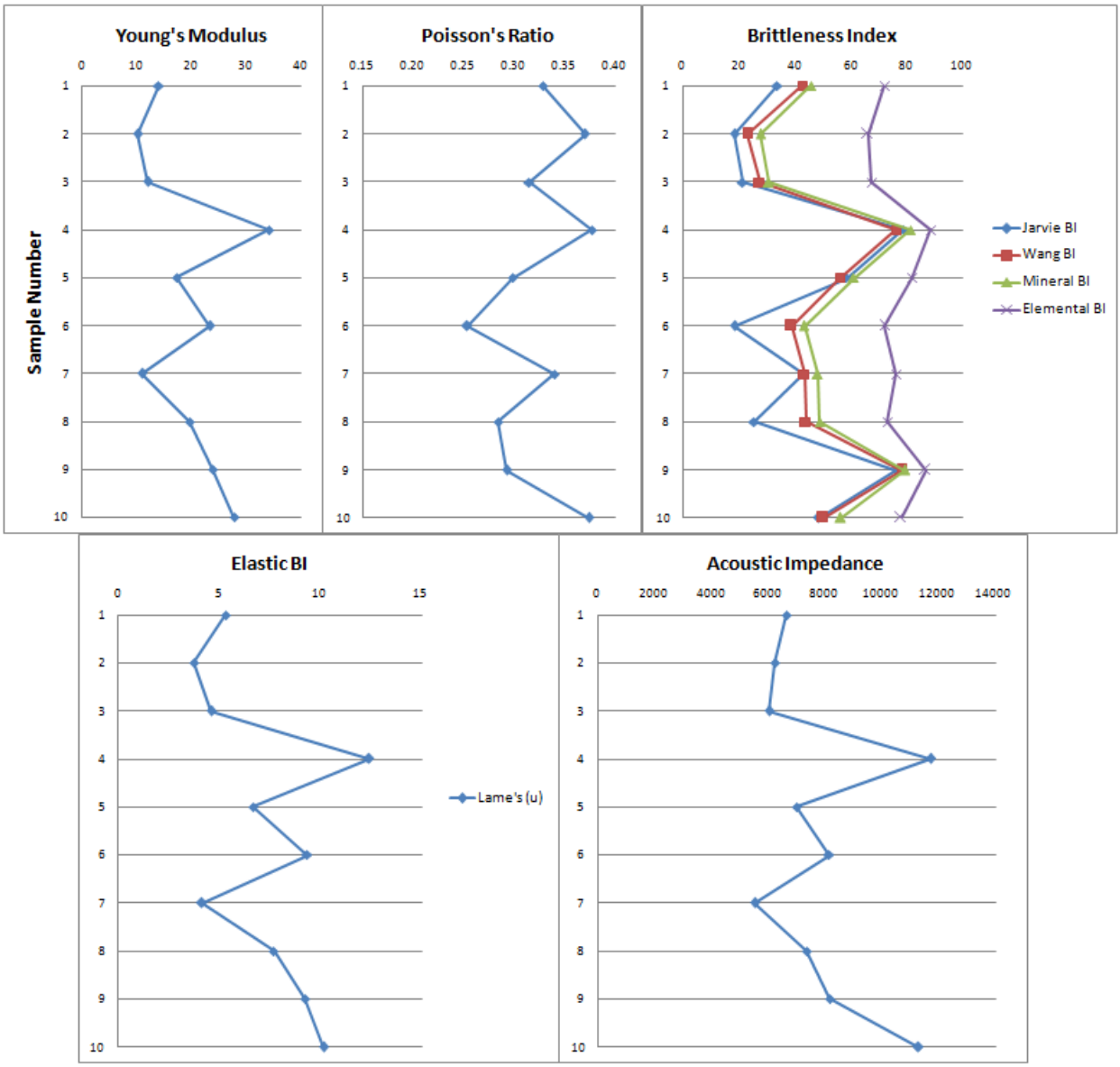

Figure 21. Correlation of elastic and mineral BI with elemental BI and elastic properties. Samples are in the same order as previous charts, sample number 1 corresponds to KC06 and 10 to OC25.

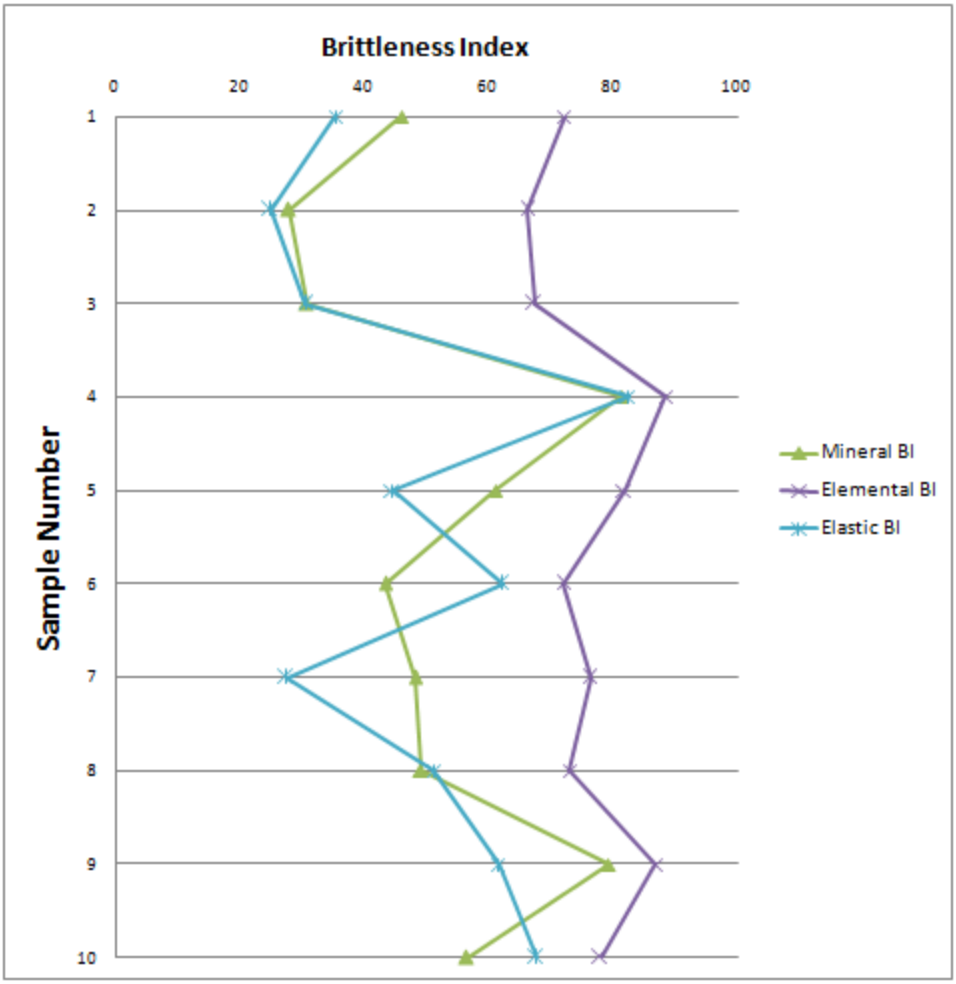

Figure 22. Correlation of elastic BI, mineral BI, and elemental BI. Samples are in the same order as previous charts, sample number 1 corresponds to KC06 and 10 to OC25.

Basin Mapping of BI

Both methods of brittleness index modeling appear to provide a reliable and relatively precise evaluation of rock properties. The development of basin-wide brittleness index maps of both elastic and mineral based BI can be developed with the addition of more samples from other studies. Examples of brittleness index maps can be seen in Figures 23 and 24. These maps can be correlated with other maps like TOC and vitrinite that have been previously developed on the Anadarko Basin.

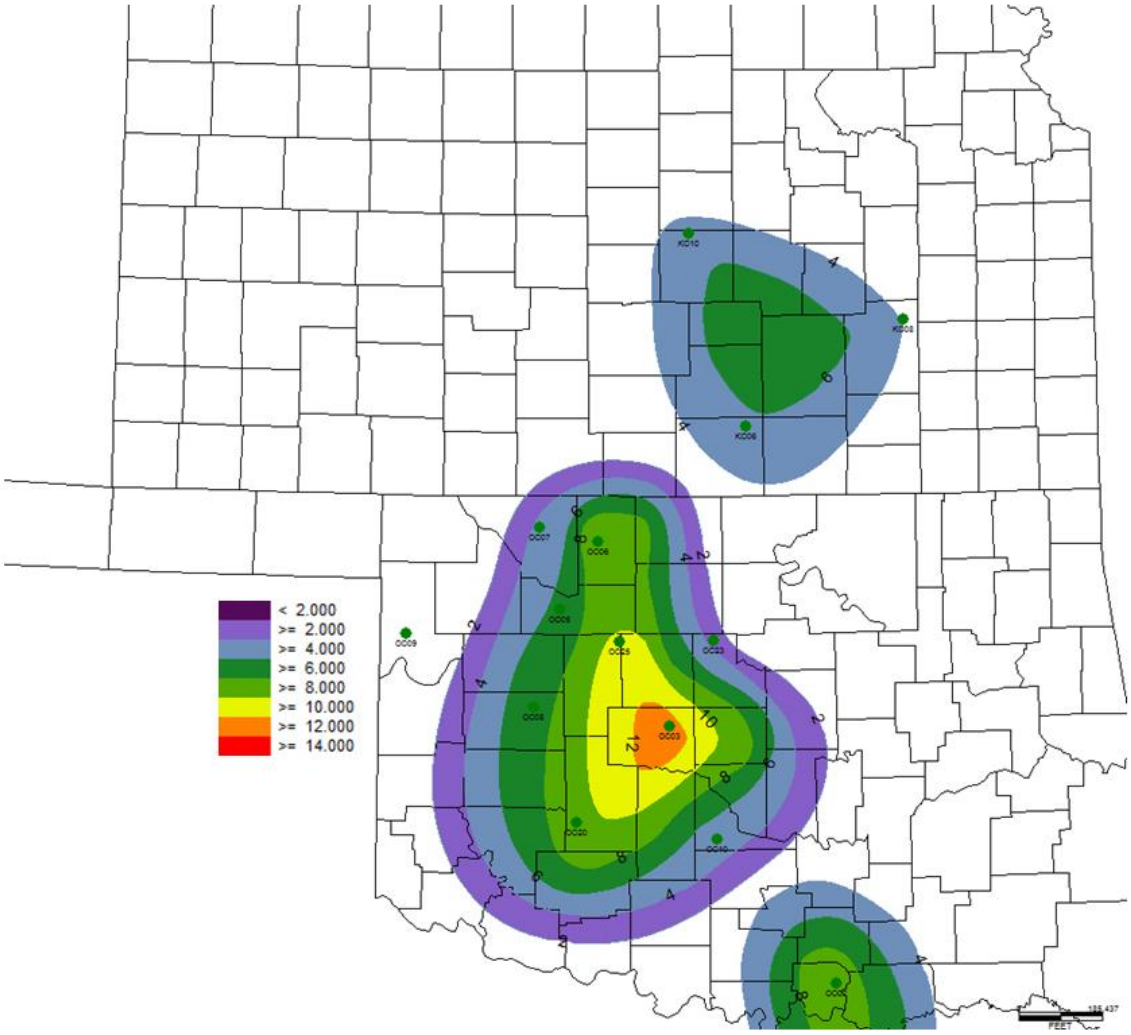

Figure 23. Elastic brittleness index contour map of Anadarko Basin based on evaluation of 13 cores.

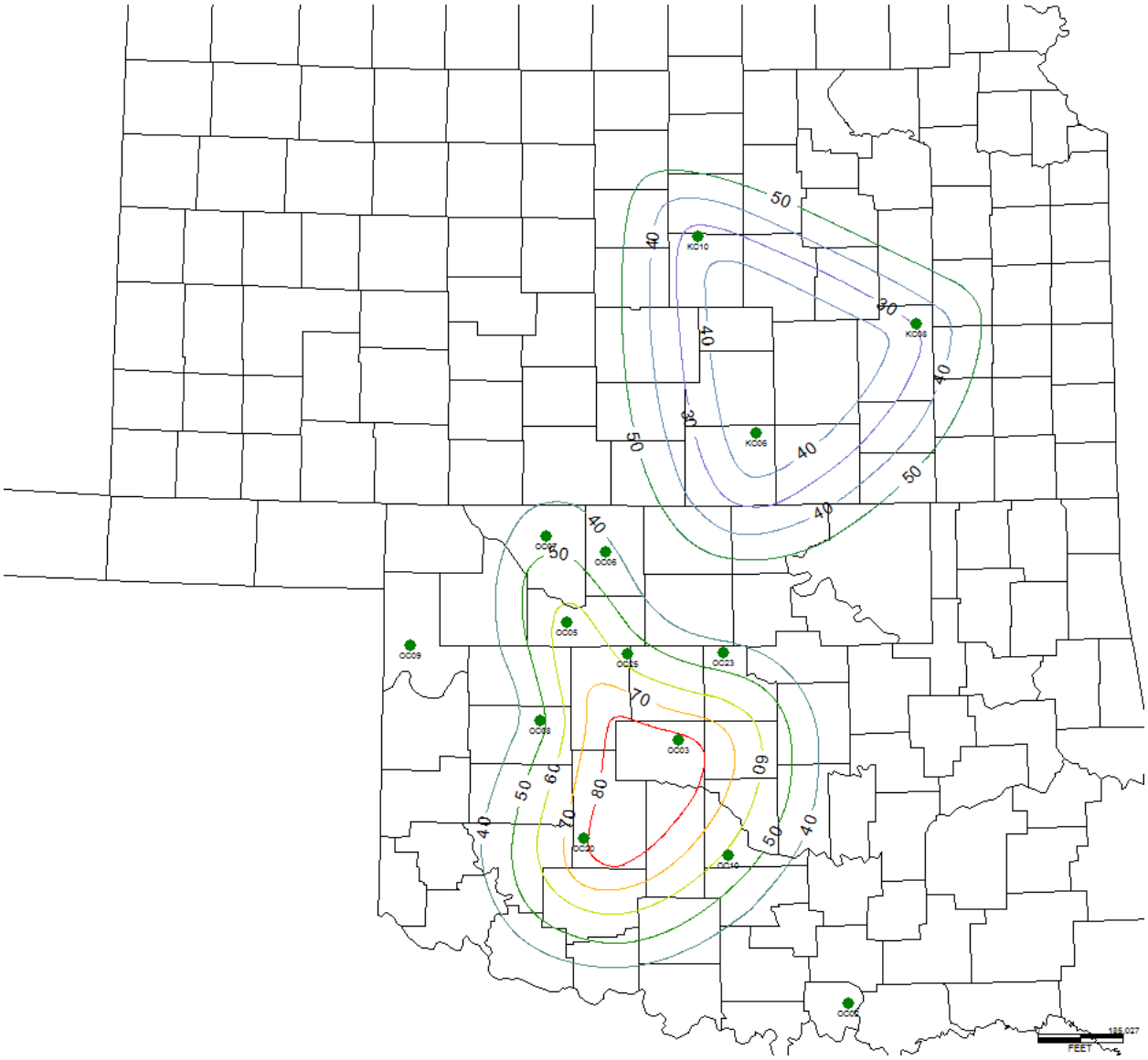

Figure 24. Mineral based brittleness index contour map of Anadarko Basin based on evaluation of 13 cores.

Figure 25 depicts further confirmation of correlation between elastic and mineral based brittleness index evaluation methods of the thirteen available Woodford cores. The elastic BI contour map was rendered partially transparent, then it was overlaid on the mineral BI contour map for comparison. The contour colors correlate relatively well indicating that the most brittle regions of the basin are located in the west-central region of Oklahoma. The TOC contour map created from the available cores correlates less well with the created brittleness index maps than

expected (Fig. 26). This lack of correlation between TOC and brittleness supports the hypothesis that TOC has little impact on elastic brittleness index.

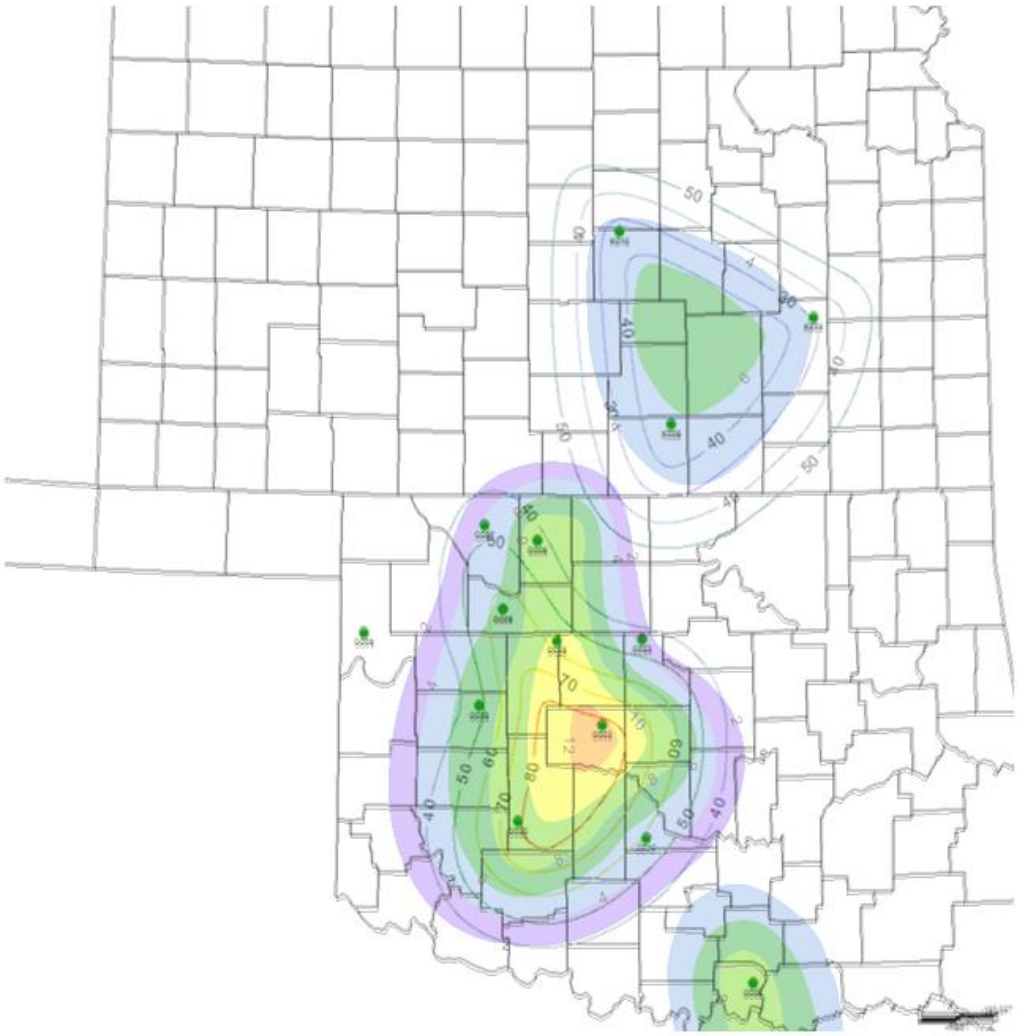

Figure 25. Correlation of elastic and mineral based brittleness index contour maps depicting the most brittle regions of the basin.

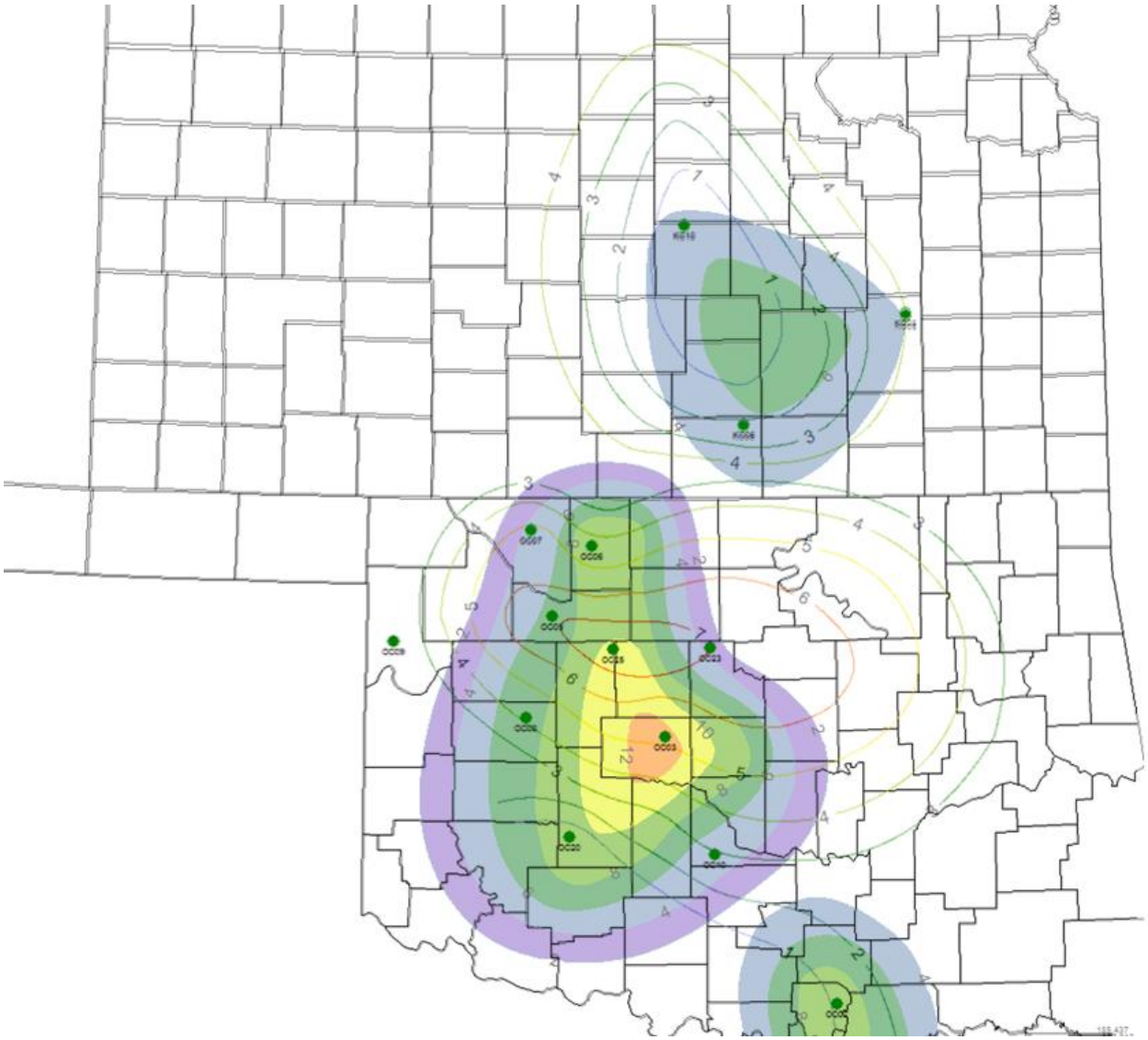

Figure 26. Correlation of TOC and elastic brittleness contour maps.

Conclusions

This study presents a rock elastic properties and mineralogy based brittleness evaluation of the Woodford Formation present in the Anadarko Basin and Kansas. Brittleness index measurements are most commonly used for evaluating the fracture potential of unconventional

reservoirs. The strongly positive correlation of the P-wave impedance of Woodford core samples to brittleness index underpins the potential of using surface seismic methods in evaluating the fracability of shale plays. While most elastic parameters provide a valid estimation of brittleness index, Lamé's parameter of rigidity (μ) has provided the most accurate estimations for the thirteen Woodford cores evaluated. While studies like those done by Wang and Gale (2009) have suggested that TOC plays a role in determining the ductile/brittle behavior of a shale, this study has shown no consistent correlation between elastic brittleness and TOC, indicating that TOC has little control on rock brittleness for these samples. One explanation for this difference may be the limited sample size processed in this study. Another complicating factor that could have effected sample processing was the varying quality, like presence of micro fractures and post core extraction age, as well as the size variations of the cores available. This may have introduced uncertainty into the velocity measurements during analysis. The presence of micro fractures can cause slower P- and S-wave velocities to be recorded, while varying sample sizes present the risk of not achieving a perfect seal with the sensors. Comparisons between brittleness and vitrinite reflectance were not possible, because the samples had limited variation in vitrinite reflectance values.

The elastic brittleness index correlates well with the mineral-based brittleness index, calculated from mineral weight percentages that were derived from XRD data and major element measurements take via XRF. Both indexes showed a positive correlation with quartz, calcite, hematite, and pyrite indicating that a larger abundance of these minerals would result in an increase of brittleness index. Strong negative correlations were also seen with clay minerals illite and kaolinite, which indicates that the presence of these minerals results in an overall decrease in brittleness.

Correlation seen between Young's Modulus, acoustic impedance, elastic BI, and mineral BI indicate that these methods may be an effective way to predict brittleness. It should be noted that brittleness index is only one of many factors for predicting the fracture potential of a reservoir.

Further Research

Upon completion of this study, further research is suggested to further validate the results found and produce a more accurate geomechanical model.

1. Reconstruct this study at conditions that are more realistic of the actual in situ conditions, along with a larger sample size containing a broader diversity of mineralogy and vitrinite values.

This would provide a better understanding of how P- and S-wave velocities would react to shales that are *in situ*. The broader diversity of mineralogy would allow for further confirmation of analyses made in this study and more diverse vitrinte values will allow the impact of vitrinte on brittleness to be analyzed.

2. Conduct further analysis with the use of CT imaging, triaxial hardness tests, and fluid content.

The information from these tests would provide information on porosity and mineral structure/alignment present in the shales. Then the impact of these factors on brittleness could be evaluated. Evaluation of how fluid content impacts brittleness will give a better understanding of shale in their actual in situ conditions.

3. Further develop the Woodford Formation brittleness index map of the Anadarko Basin.

This is suggested in the hopes of developing a comprehensive brittleness index map for the full extent of the Woodford formation.

References

Altamar, R.P., Marfurt, K., (2014). Mineralogy-based brittleness prediction from surface seismic data: Application to the Barnett Shale. Interpretation, 2(4), T255-T271.

Ball, M.M., Henry, M.E., and Frezon S.E., (1991). Petroleum Geology of the Anadarko Basin Region, Province (115), Kansas, Oklahoma, and Texas. U.S. Geological Survey, Open-File Report 88-450W. http://pubs.usgs.gov/of/1988/0450w/report.pdf.

Cardott, B.J., and Lambert, M.W., (1985). Thermal maturation by vitrinite reflectance of Woodford Shale, Anadarko Basin, Oklahoma. AAPG Bull., 69, 1982-1998.

Coddington, K., (2013). The Role of Heavy Minerals in the Thermal Maturation of the Woodford Shale, Anadarko Basin, Oklahoma. Thesis. Kansas State University Graduate School, 2013. Manhattan. Kansas State University.

Energy Information Administration (EIA) (2011a). Shale Gas is a Global Phenomenon. Today in Energy, http://www.eia.gov/todayinenergy/detail.cfm?id=811, accessed September 12, 2014.

Feinstein, S., (1981). Subsidence and thermal history of Southern Oklahoma aulacogen Implications for petroleum exploration: American Association of Petroleum Geologists Bulletin, v. 65, p. 2531-2533.

Goodway, B., Varsek, J., and Abaco, C., (2007). Isotropic AVO methods to detect fracture prone zones in tight gas resouce plays. 2007 CSPG CSEG Convention, 586-589.

Grieser, B., and Bray, J., (2007). Identification of production potential in unconventional reservoirs: Proceedings of the Annual Technical Conference and Exhibition, Society of Petroleum Engineers, SPE 106623.

Guo ZQ, Li XY, Liu C., (2013) A shale rock physics model for analysis of brittleness index, mineralogy and porosity in the Barnett Shale. Journal of Geophysics and Engineering 10: 1–10.

Gupta, N., Sarkar, S., and Marfurt, K., (2013). Seismic Attribute Driven Integration Characterization of the Woodford Shale in West-Central Oklahoma. Interpretation [Tulsa], 1 (2), 85-96.

Higley, D.K., (2014). Thermal Maturation of Petroleum Source Rocks in the Anadarko Basin Province, Colorado, Kansas, Oklahoma, and Texas, chap. 3, *in* Higley, D.K., compiler, Petroleum systems and assessment of undiscovered oil and gas in the Anadarko Basin Province, Colorado, Kansas, Oklahoma, and Texas ---USGS Province 58: U.S. Geological Survey Digital Data Series DDS-69-EE, 53 p., *http://dx.doi.org/10.3133/ds69EE.*

Hu, R., Vernik, L., Nayvelt, L., and Dicman, A., (2015). Seismic Inversion for Organic Richness and Fracture Gradient in Unconventional Reservoirs: Eagle Ford Shale, Texas. The Leading Edge, 34(1), 80-82, 84.

Jaiswal, P., Varacchi, B., Ebrahimi, P., Dvorkin, J., and Puckette, J., (2014). Can seismic velocities predict sweet spots in the Woodford Shale? A case study from MCNeff 2-28 Well, Grady County, Oklahoma. Journal of Applied Geophysics, 104, 26-34.

Jarvie, D. M., Hill, R. J., Ruble, T. E., and Pollastro, R. M., (2007). Unconventional shale-gas systems: The Mississippian Barnett Shale of North-Central Texas as one model for thermogenic shale-gas assessment: AAPG Bulletin, 91, 475–499.

Johnson, K. S., and Cardott, B.J., (1992). Geologic Framework and Hydrocarbon Source Rocks of Oklahoma. Oklahoma Geological Survey Circular ,93 (21), 37.

Johnson, K. S., Amsden, T.W., Denison, R.E., Goldstein, A.G., Dutton, S.P., Rascoe, J.B., Sutherland, P.K., and Thompson, C.M., (1989). Geology of the Southern Midcontinent. Oklahoma Geological Survey Special Publication, 89, (2), 1-53.

Janssen, Kale, (2017). A study of the effects of organic matter on illitization in the Woodford shale, Oklahoma and Kansas. Thesis. Kansas State University Graduate School, 2017. Manhattan. Kansas State University.

Herwanger, J.; Bottrill, A. and Mildren, S., (2015). Uses and abuses of the Brittleness Index with applications to Hydraulic Stimulation. Soc. Of Petroleum Engineers, SPE-URTeC-2172545.

Kennedy, M., (2013). Clay Mineralogy Provides a First Order Control on TOC, Spatial Distribution of Organic Enrichment, Fracability and Diagenesis in the Woodford, Green River, Monterey and Pierre Shale, USA. International Geological Congress, Abstracts, 34, 2680.

Lambert, M.W., (1993). Internal Stratigraphy and Organic Facies of the Devonian-Mississippian Chattanooga (Woodford) Shale in Oklahoma and Kansas, *in* B.J. Katz and L.M. Pratt, eds., Source rocks in a sequence stratigraphic framework: AAPG Studies in Geology 37, p. 163-176.

Rivera, K.T., Puckette, J., and Quan, T.M., (2015). Evaluation of redox versus thermal maturity controls on $\delta^{15}N$ in organic rich shales: A case study of the Woodford Shale, Anadarko Basin, Oklahoma, USA. Organic Chemistry, 83-84 (1), 127-139.

Totten, M.W.,and Blatt, H., 1996, Sources of Silica During Late-Diagenesis of Shales from the Ouachita Mountains, Oklahoma and Arkansas: in Crossey, L.J., Loucks, R. and, Totten, M.W., eds.: Siliciclastic Diagenesis and Fluid Flow: Concepts and Applications, SEPM Special Publication 55, p. 78-85.

Wang, F. P., and Gale, J. F. W., (2009). Screening criteria for shale-gas systems: Gulf Coast Association of Geological Societies Transactions, 59, 779–793.

Whitmeyer, S. J. & Karlstrom, K. E. Tectonic model for the Proterozoic growth of North America. Geosphere **3**, 220–259 (2007).

Xu, J., and Sonnenberg, S., (2016) Brittleness and Rock Strength of the Bakken Formation, Williston Basin, North Dakota. Unconventional Resources Technology Conference, San Antonia, Texas, 1-3 August 2016: pp. 2237-2254.

Appendix

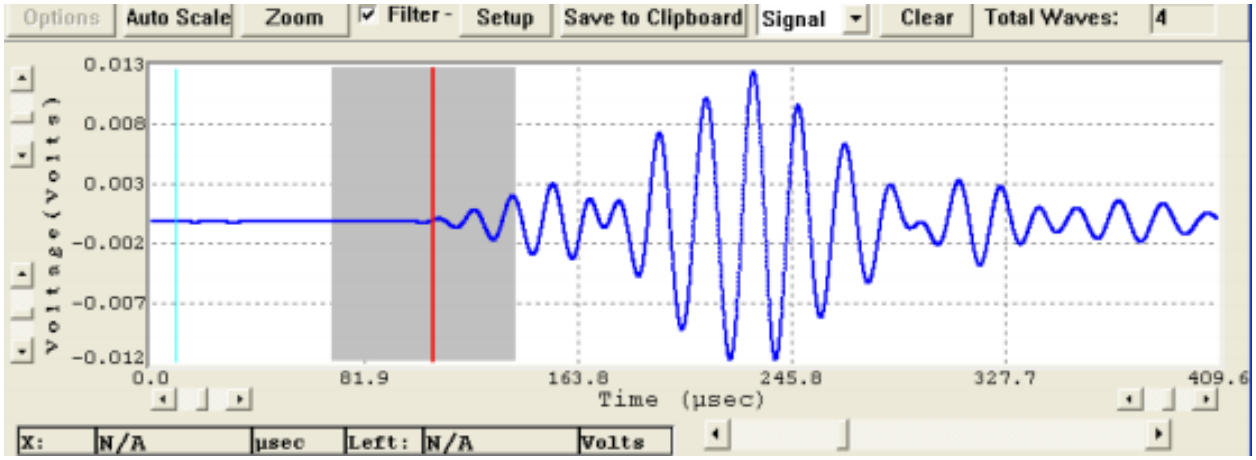

Figure A-1. GCTS Ultrasonic Velocity Software voltage vs time graph.

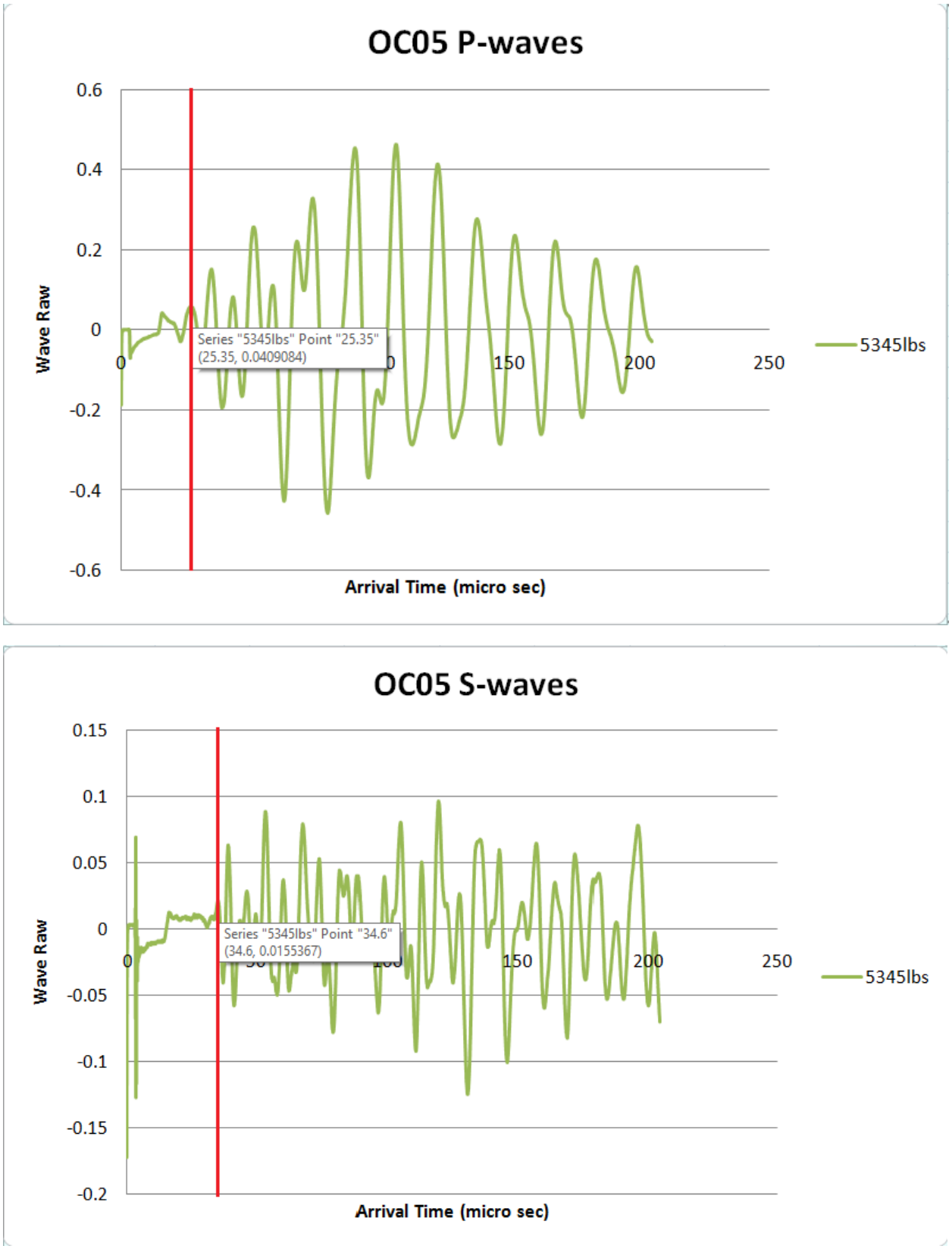

Figure A-2. Example of P- and S-wave first arrival time picks from Excel.

Sample	AlKa1	SiKa1	P Ka1	S Ka1	K Ka1	CaKa1	TiKa1	V Ka1	CrKa1	MnKa1	FeKa1
KC06	6.46	20.58	0.03	0.98	3.67	1.67	0.43	0.01	0.01	0.03	3.81
KC08	6.17	16.22	0.03	1.04	4.54	0.84	0.44	0.02	0.01	0.03	3.79
KC10	6.42	16.52	0.03	0.76	4.15	0.98	0.45	0.01	0.01	0.03	4.24
OC02	1.43	20.50	0.06	0.36	0.95	6.82	0.15	0.01	0.01	0.03	0.89
OC03	2.89	31.34	0.04	0.85	1.45	0.34	0.21	0.06	0.01	0.03	1.15
OC05	3.21	24.48	0.04	0.46	2.59	0.23	0.28	0.09	0.01	0.02	1.34
OC06	5.14	15.54	0.03	1.43	3.90	3.66	0.36	0.01	0.01	0.04	3.94
OC07	4.41	20.11	0.02	0.97	3.01	0.39	0.32	0.03	0.01	0.02	3.22
OC08	4.93	17.31	0.02	1.90	3.82	3.31	0.37	0.04	0.01	0.03	2.96
OC20	3.48	31.36	0.05	0.85	1.60	0.44	0.23	0.03	0.02	0.03	1.32
OC25	5.19	22.28	0.12	4.66	2.95	0.22	0.31	0.02	0.01	0.02	6.16

Table A-1. XRF major element weight percentages BI for 11 of the 13 Woodford core samples.

KC06				
mineral	Ele. Prop.	mineral ml. mass	mineral wt.	mineral wt. %
illite(KAl2(Si,Al)4O10)	7.72	389.00	3002.22	45.78
pyrite(FeS2)	1.25	119.98	150.51	2.30
apatite(Ca5(PO4)3(OH,F,Cl))	0.03	509.00	12.83	0.20
fe-ti oxides(FeTiO3)	0.73	151.70	111.14	1.69
dolomite((Ca,Mg) CO3)	3.36	184.40	618.89	9.44
chlorite((Mg, Fe)4Al4Si2O10(OH)8)	0.91	595.00	540.20	8.24
quartz(SiO2)	35.31	60.08	2121.59	32.35
		total	**6557.38**	
KC08				
mineral	Ele. Prop.	mineral ml. mass	mineral wt.	mineral wt. %
illite(KAl2(Si,Al)4O10)	11.01	389.00	4283.21	63.34
pyrite(FeS2)	1.54	119.98	185.25	2.74
apatite(Ca5(PO4)3(OH,F,Cl))	0.03	509.00	14.35	0.21
fe-ti oxides(FeTiO3)	0.88	151.70	133.40	1.97
dolomite((Ca,Mg) CO3)	1.94	184.40	358.43	5.30
chlorite((Mg, Fe)4Al4Si2O10(OH)8)	1.00	595.00	597.72	8.84
quartz(SiO2)	19.80	60.08	1189.70	17.59
		total	**6762.04**	
KC10				
mineral	Ele. Prop.	mineral ml. mass	mineral wt.	mineral wt. %
illite(KAl2(Si,Al)4O10)	9.95	389.00	3871.81	57.78
pyrite(FeS2)	1.11	119.98	132.65	1.98
apatite(Ca5(PO4)3(OH,F,Cl))	0.03	509.00	17.18	0.26
fe-ti oxides(FeTiO3)	0.87	151.70	132.59	1.98
dolomite((Ca,Mg) CO3)	2.25	184.40	414.57	6.19
chlorite((Mg, Fe)4Al4Si2O10(OH)8)	1.29	595.00	765.14	11.42
quartz(SiO2)	22.75	60.08	1366.80	20.40
		total	**6700.74**	
OC02				
mineral	Ele. Prop.	mineral ml. mass	mineral wt.	mineral wt. %
illite(KAl2(Si,Al)4O10)	2.40	389.00	935.15	11.47
pyrite(FeS2)	0.56	119.98	67.20	0.82
apatite(Ca5(PO4)3(OH,F,Cl))	0.07	509.00	33.97	0.42
fe-ti oxides(FeTiO3)	0.32	151.70	48.30	0.59
dolomite((Ca,Mg) CO3)	16.59	184.40	3058.98	37.53
chlorite((Mg, Fe)4Al4Si2O10(OH)8)	0.18	595.00	104.48	1.28
quartz(SiO2)	64.95	60.08	3902.36	47.88
		total	**8150.45**	

Table A-2. Mineral weight percentage calculations for samples KC06, KC08, KC10, and OC02.

OC03				
mineral	Ele. Prop.	mineral ml. mass	mineral wt.	mineral wt. %
illite(KAl2(Si,Al)4O10)	2.80	389.00	1088.17	18.17
pyrite(FeS2)	1.00	119.98	120.09	2.00
apatite(Ca5(PO4)3(OH,F,Cl))	0.04	509.00	18.36	0.31
fe-ti oxides(FeTiO3)	0.33	151.70	49.74	0.83
dolomite((Ca,Mg) CO3)	0.62	184.40	114.26	1.91
chlorite((Mg, Fe)4Al4Si2O10(OH)8)	0.06	595.00	35.15	0.59
quartz(SiO2)	75.96	60.08	4563.81	76.20
		total	**5989.58**	
OC05				
mineral	atomic wt. %	mineral ml. mass	mineral wt.	mineral wt. %
illite(KAl2(Si,Al)4O10)	5.99	389.00	2328.43	36.60
pyrite(FeS2)	0.65	119.98	77.47	1.22
apatite(Ca5(PO4)3(OH,F,Cl))	0.04	509.00	20.19	0.32
fe-ti oxides(FeTiO3)	0.52	151.70	79.57	1.25
dolomite((Ca,Mg) CO3)	0.49	184.40	91.14	1.43
chlorite((Mg, Fe)4Al4Si2O10(OH)8)	0.25	595.00	147.09	2.31
quartz(SiO2)	60.21	60.08	3617.68	56.87
		total	**6361.56**	
OC06				
mineral	Ele. Prop.	mineral ml. mass	mineral wt.	mineral wt. %
illite(KAl2(Si,Al)4O10)	9.45	389.00	3675.43	48.91
pyrite(FeS2)	2.11	119.98	252.63	3.36
apatite(Ca5(PO4)3(OH,F,Cl))	0.03	509.00	13.55	0.18
fe-ti oxides(FeTiO3)	0.71	151.70	108.36	1.44
dolomite((Ca,Mg) CO3)	8.47	184.40	1562.60	20.79
chlorite((Mg, Fe)4Al4Si2O10(OH)8)	0.96	595.00	573.97	7.64
quartz(SiO2)	22.10	60.08	1327.82	17.67
		total	**7514.35**	
OC07				
mineral	atomic wt. %	mineral ml. mass	mineral wt.	mineral wt. %
illite(KAl2(Si,Al)4O10)	7.25	389.00	2819.84	43.98
pyrite(FeS2)	1.42	119.98	170.78	2.66
apatite(Ca5(PO4)3(OH,F,Cl))	0.02	509.00	10.96	0.17
fe-ti oxides(FeTiO3)	0.64	151.70	96.62	1.51
dolomite((Ca,Mg) CO3)	0.91	184.40	167.13	2.61
chlorite((Mg, Fe)4Al4Si2O10(OH)8)	0.84	595.00	501.32	7.82
quartz(SiO2)	44.04	60.08	2645.67	41.26
		total	**6412.31**	

Table A-3. Mineral weight percentage calculations for samples OC03-07.

OC08				
mineral	Ele. Prop.	mineral ml. mass	mineral wt.	mineral wt. %
illite(KAl2(Si,Al)4O10)	8.89	389.00	3458.52	48.06
pyrite(FeS2)	2.70	119.98	324.37	4.51
apatite(Ca5(PO4)3(OH,F,Cl))	0.02	509.00	8.05	0.11
fe-ti oxides(FeTiO3)	0.70	151.70	106.41	1.48
dolomite((Ca,Mg) CO3)	7.38	184.40	1361.70	18.92
chlorite((Mg, Fe)4Al4Si2O10(OH)8)	0.36	595.00	212.00	2.95
quartz(SiO2)	28.71	60.08	1725.03	23.97
		total	7196.08	
OC20				
mineral	atomic wt. %	mineral ml. mass	mineral wt.	mineral wt. %
illite(KAl2(Si,Al)4O10)	3.02	389.00	1174.65	19.67
pyrite(FeS2)	0.97	119.98	116.80	1.96
apatite(Ca5(PO4)3(OH,F,Cl))	0.04	509.00	20.81	0.35
fe-ti oxides(FeTiO3)	0.36	151.70	54.24	0.91
dolomite((Ca,Mg) CO3)	0.78	184.40	143.76	2.41
chlorite((Mg, Fe)4Al4Si2O10(OH)8)	0.10	595.00	61.78	1.03
quartz(SiO2)	73.22	60.08	4398.77	73.67
		total	5970.82	
OC25				
mineral	Ele. Prop.	mineral ml. mass	mineral wt.	mineral wt. %
illite(KAl2(Si,Al)4O10)	5.66	389.00	2202.62	37.41
pyrite(FeS2)	5.45	119.98	653.88	11.11
apatite(Ca5(PO4)3(OH,F,Cl))	0.10	509.00	50.32	0.85
fe-ti oxides(FeTiO3)	0.48	151.70	73.10	1.24
dolomite((Ca,Mg) CO3)	0.39	184.40	72.57	1.23
chlorite((Mg, Fe)4Al4Si2O10(OH)8)	0.59	595.00	348.21	5.91
quartz(SiO2)	41.38	60.08	2486.39	42.23
		total	5887.10	

Table A-4. Mineral weight percentage calculations for samples OC08, OC20, and OC25.

			Wt % of calculated mineralogy					
Sample	illite	pyrite	FeTi oxides	apatite	chlorite	dolomite	qtz/chert/fossil tests	Mineral BI
KC06	45.78	2.30	1.69	0.20	8.24	9.44	32.35	45.87
KC08	63.34	2.74	1.97	0.21	8.84	5.30	17.59	27.67
KC10	57.78	1.98	1.98	0.26	11.42	6.19	20.40	30.62
OC02	11.47	0.82	0.59	0.42	1.28	37.53	47.88	55.65
OC03	18.17	2.00	0.83	0.31	0.59	1.91	76.20	81.19
OC05	36.60	1.22	1.25	0.32	2.31	1.43	56.87	60.96
OC06	48.91	3.36	1.44	0.18	7.64	20.79	17.67	43.35
OC07	43.98	2.66	1.51	0.17	7.82	2.61	41.26	48.12
OC08	48.06	4.51	1.48	0.11	2.95	18.92	23.97	48.94
OC20	19.67	1.96	0.91	0.35	1.03	2.41	73.67	79.22
OC25	37.41	11.11	1.24	0.85	5.91	1.23	42.23	56.30

Table A-5. Calculated mineralogy and mineral-based brittleness index of all 11 samples.

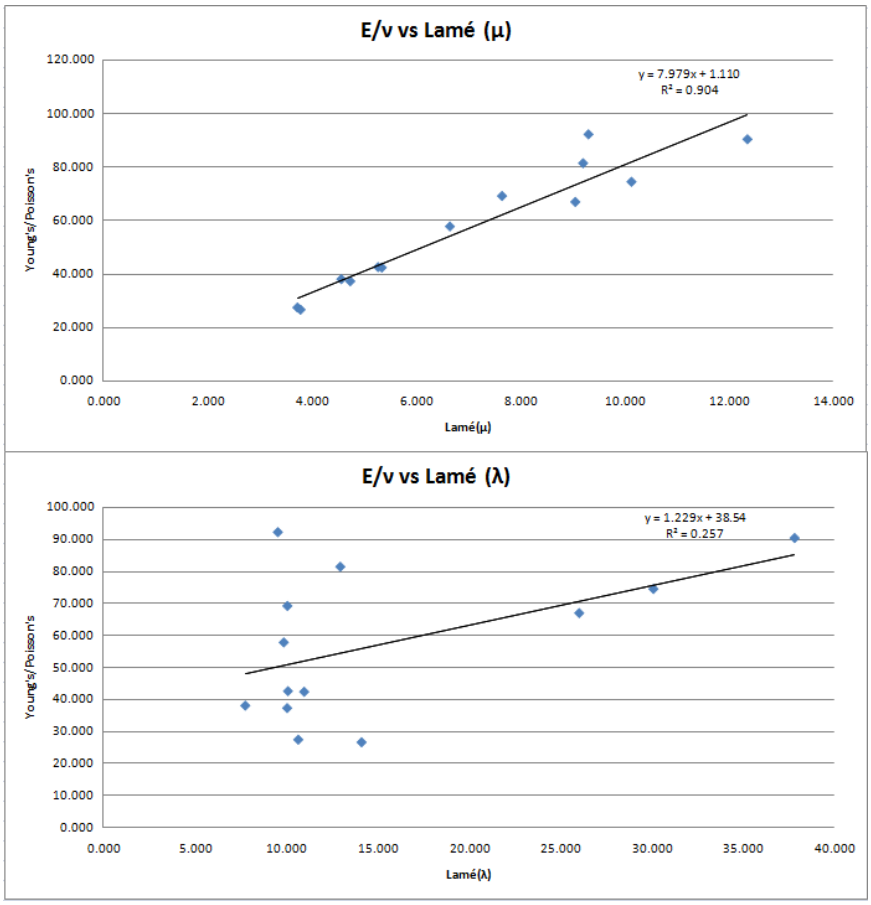

Figure A-3. Lamé parameters (μ) and (λ) vs E/ν depicting that rigidity (μ) has a better fit.

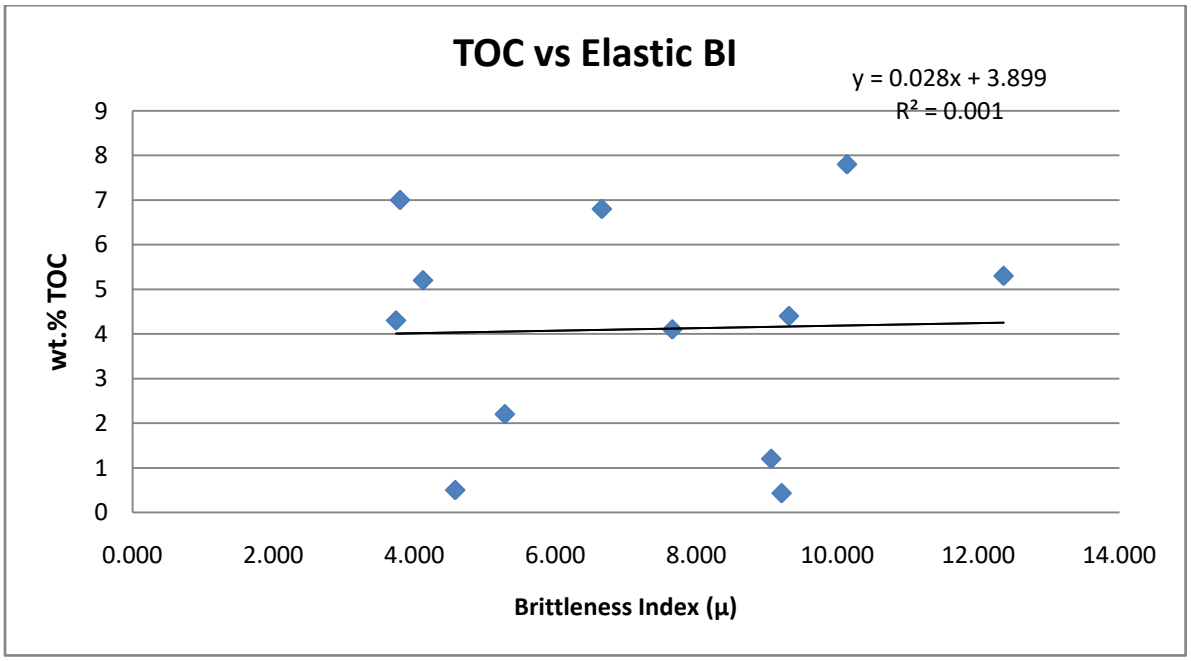

Figure A-4. Graph depicting lack of correlation between TOC and elastic BI .

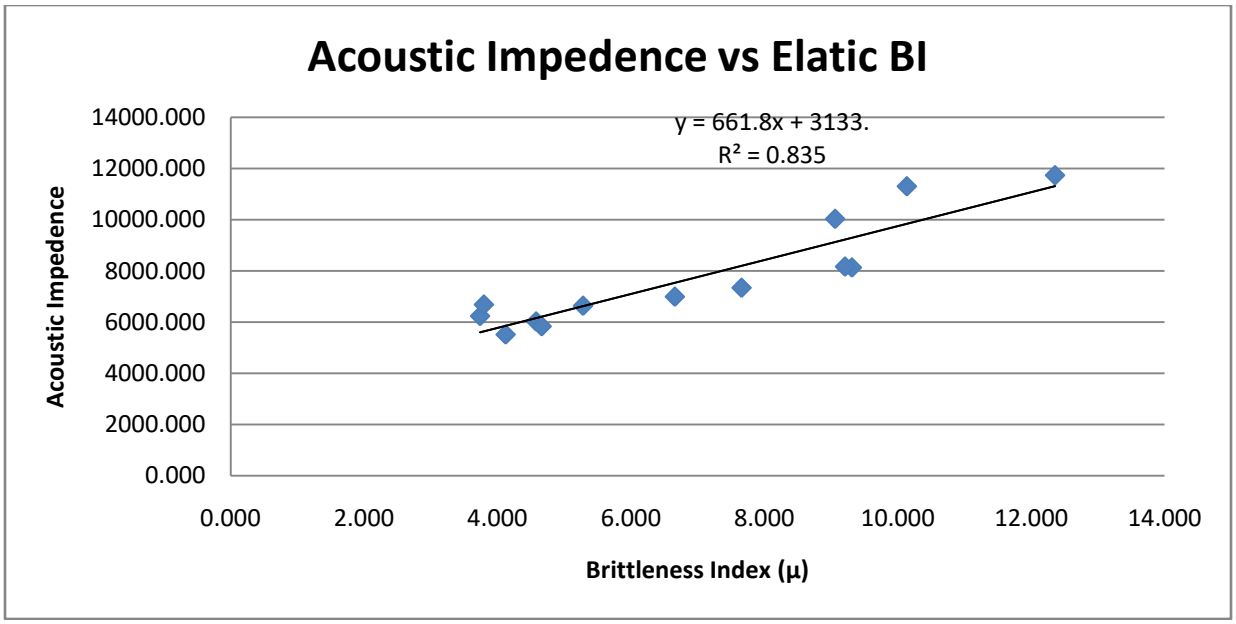

Figure A-5. Graphs depicting correlation of acoustic impedance with elastic brittleness.

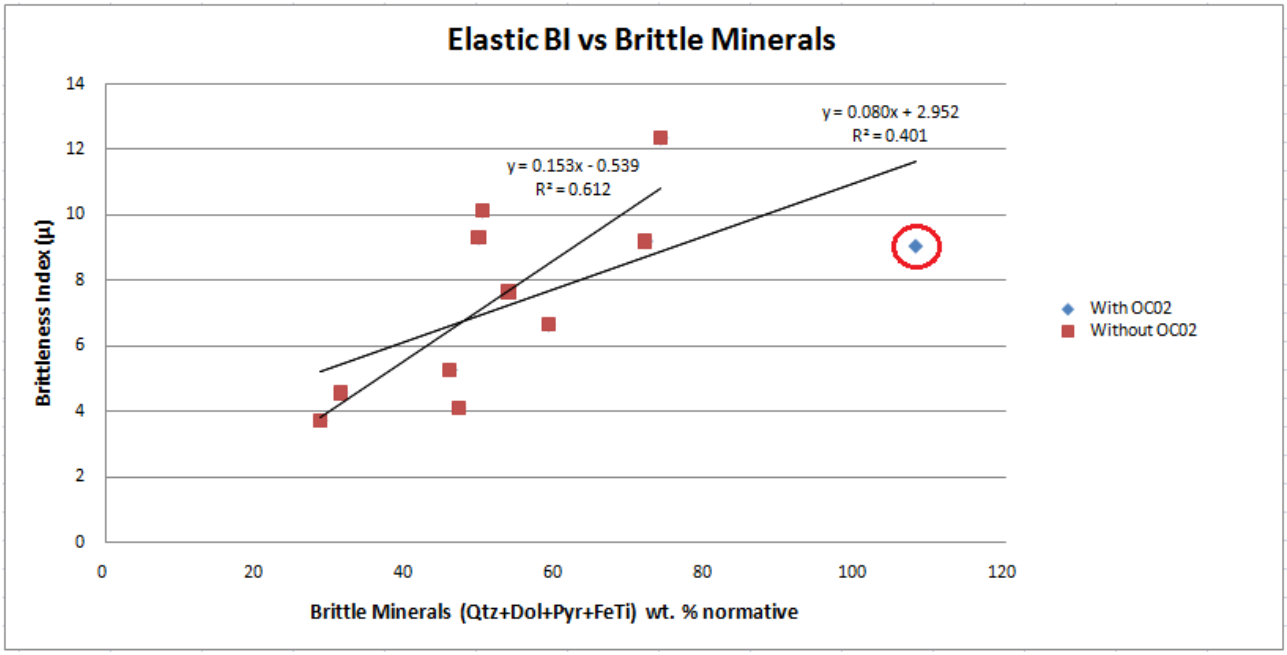

Figure A-6. Graphs depicting correlations with OC02 present and without. Sample OC02 is circle in red.

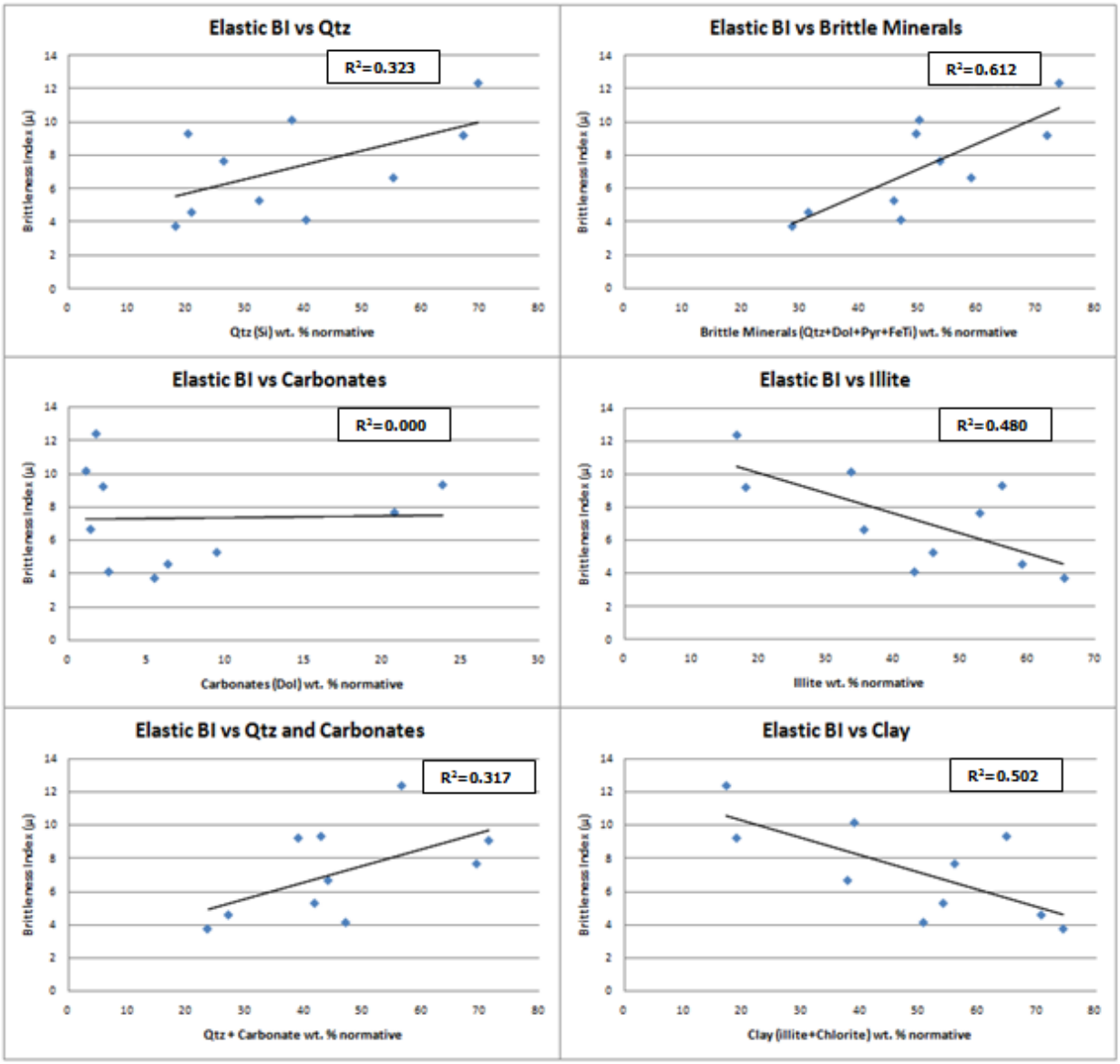

Figure A-7. Impact of calculated mineral weight percentages on the elastic BI of the Woodford shale.

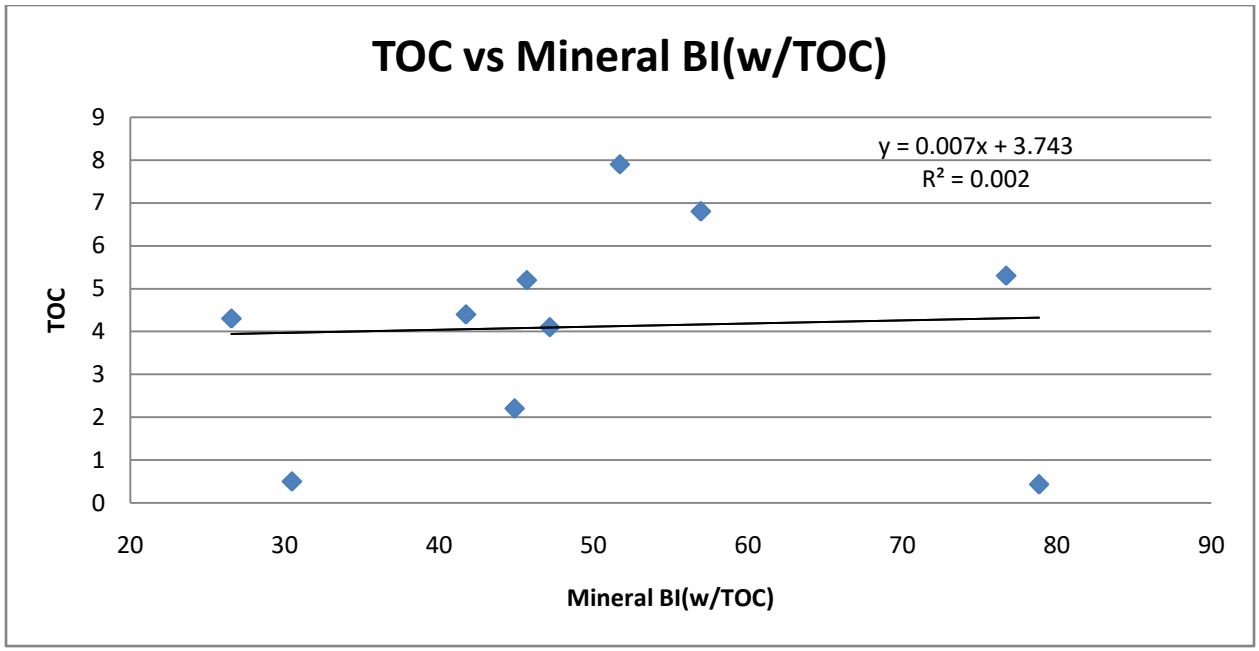

Figure A-8. Graph of TOC vs mineral BI calculated with TOC. No correlation between TOC and mineral BI is seen.

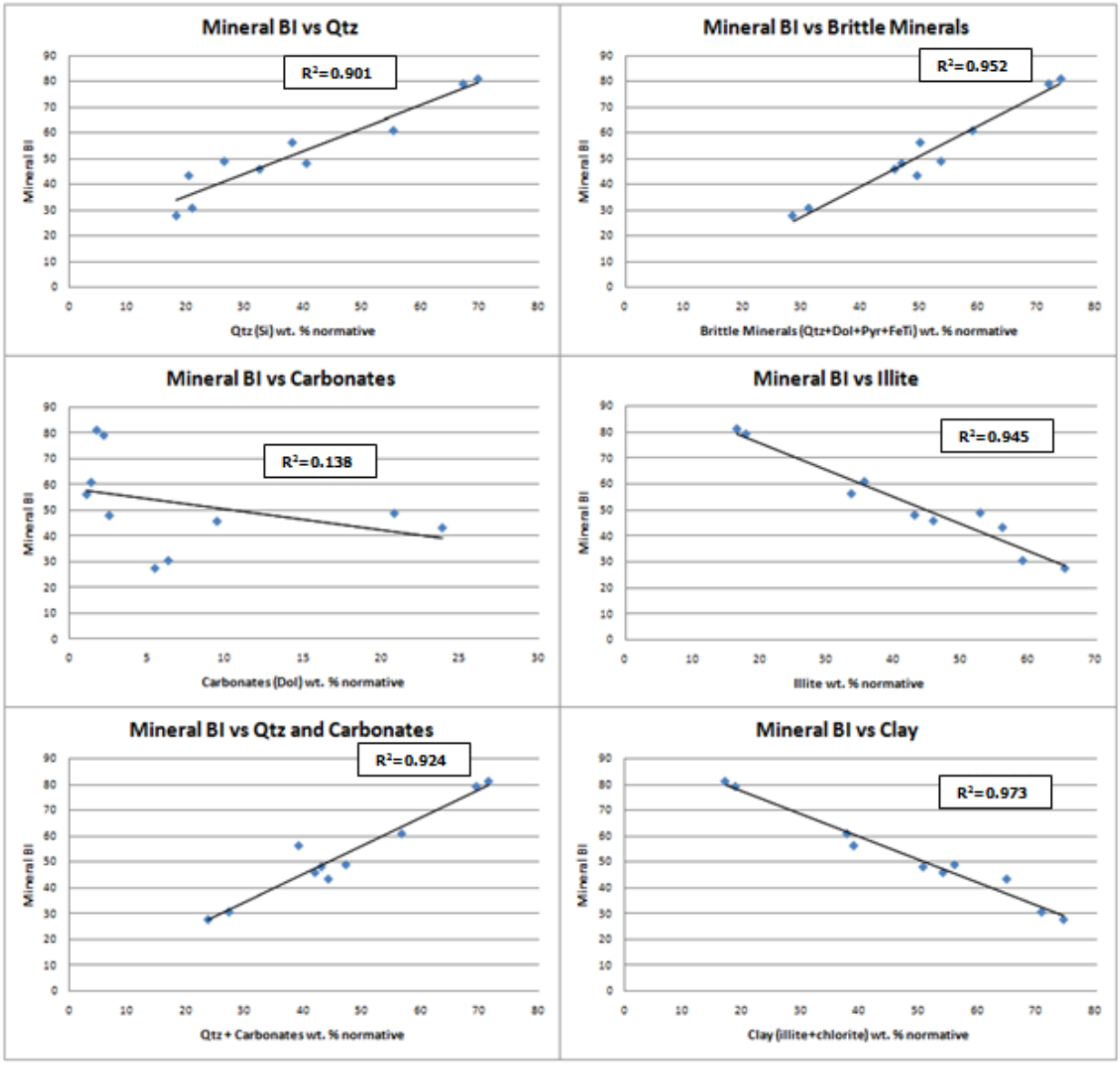

Figure A-9. Impact of calculated mineral weight percentages on the mineral BI of the Woodford shale.

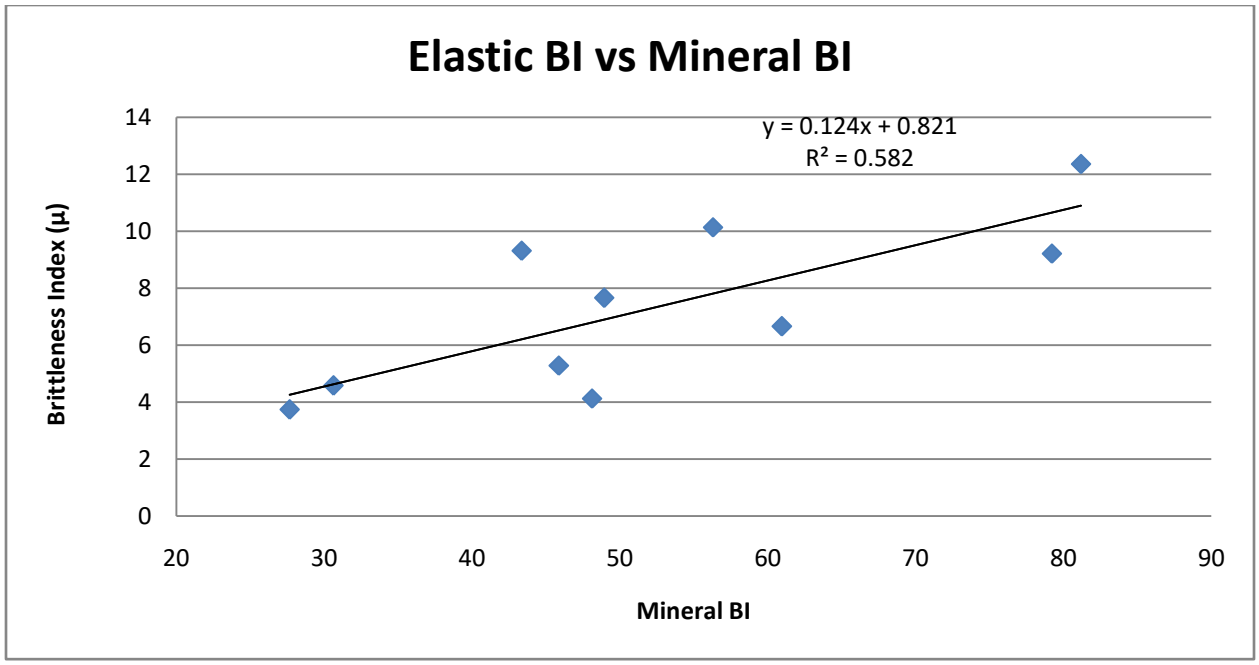

Figure A-10. Graph depicting the correlation between the elastic BI and mineral BI.

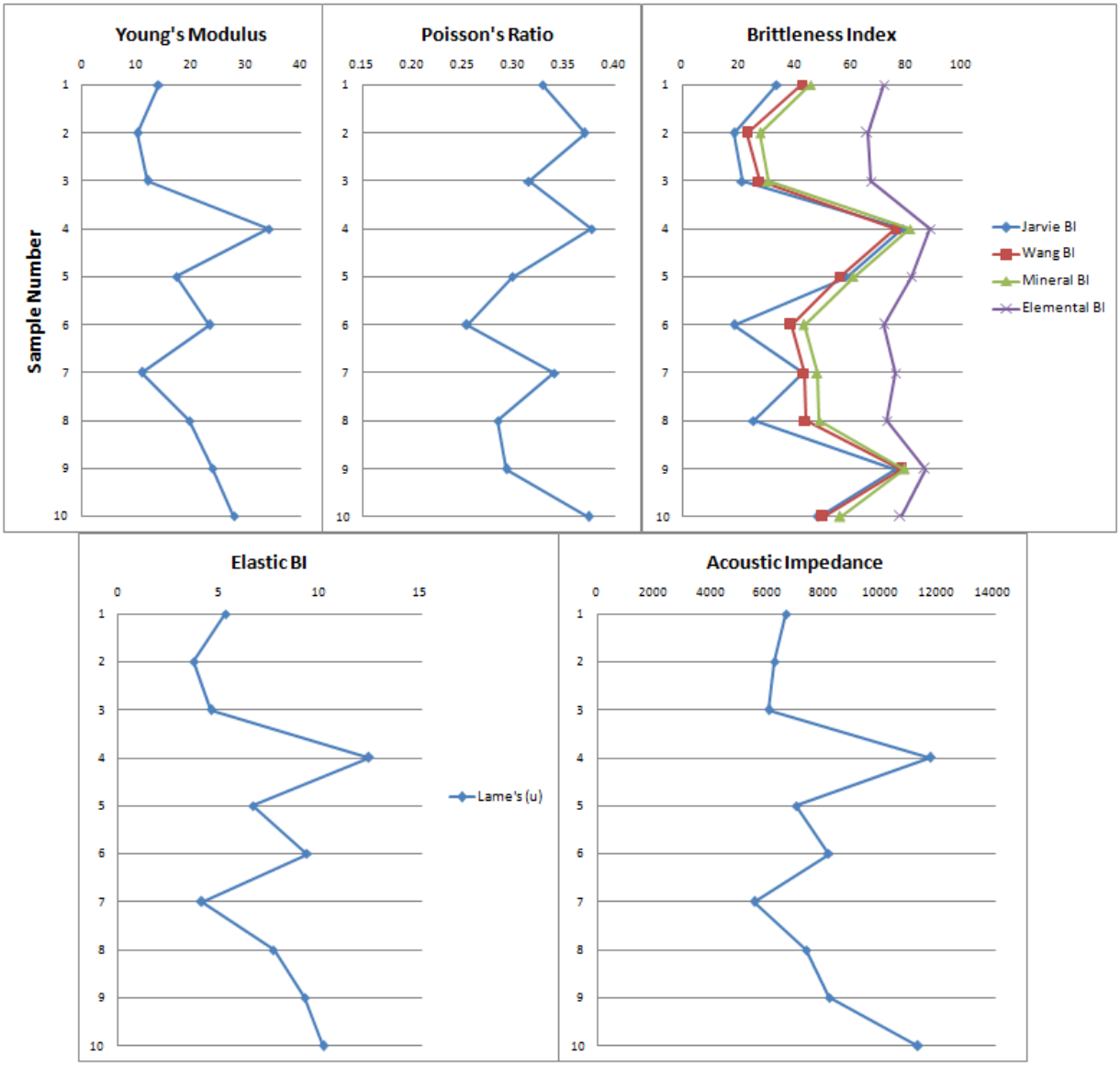

Figure A-11. Correlation of elastic and mineral BI with elemental BI and elastic properties. Samples are in the same order as previous charts, sample number 1 corresponds to KC06 and 10 to OC25.

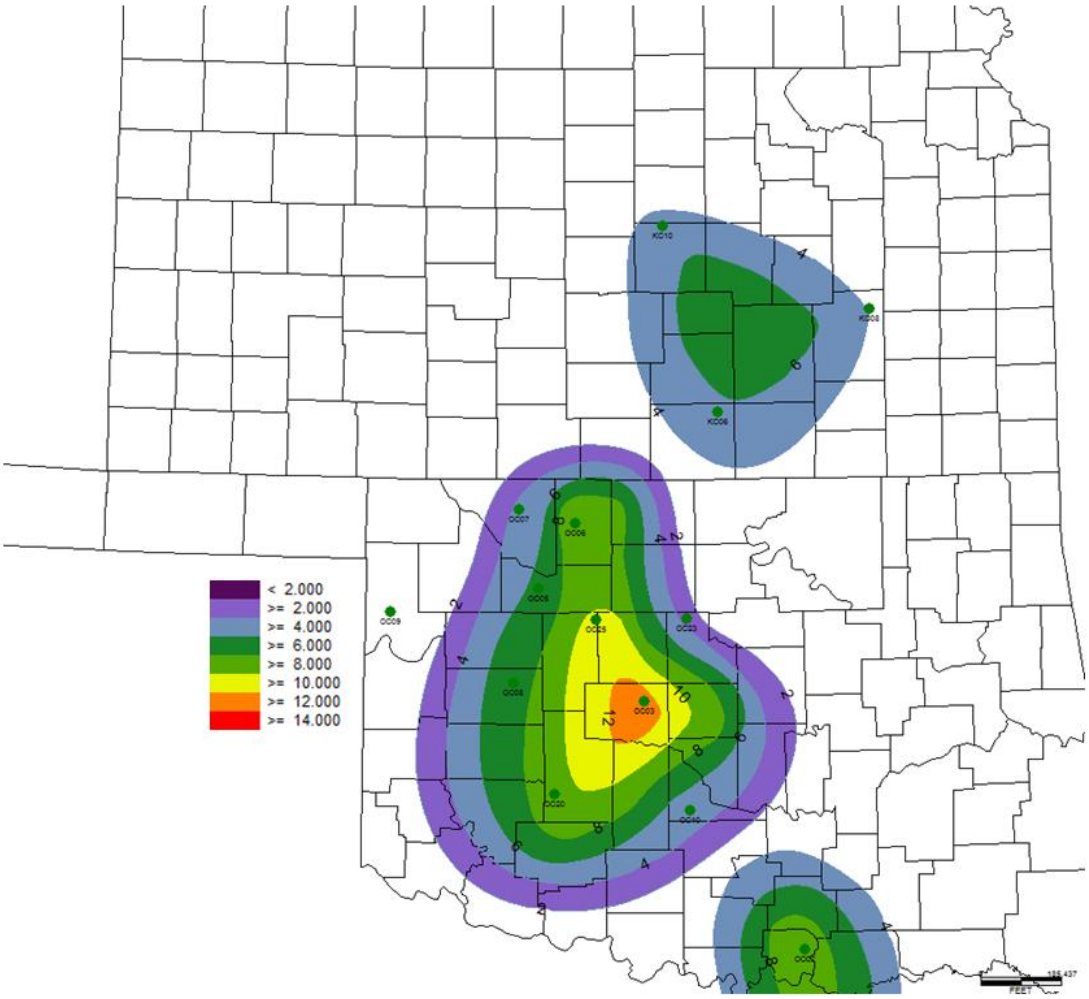

Figure A-12. Elastic brittleness index contour map of Anadarko Basin based on evaluation of 13 cores.

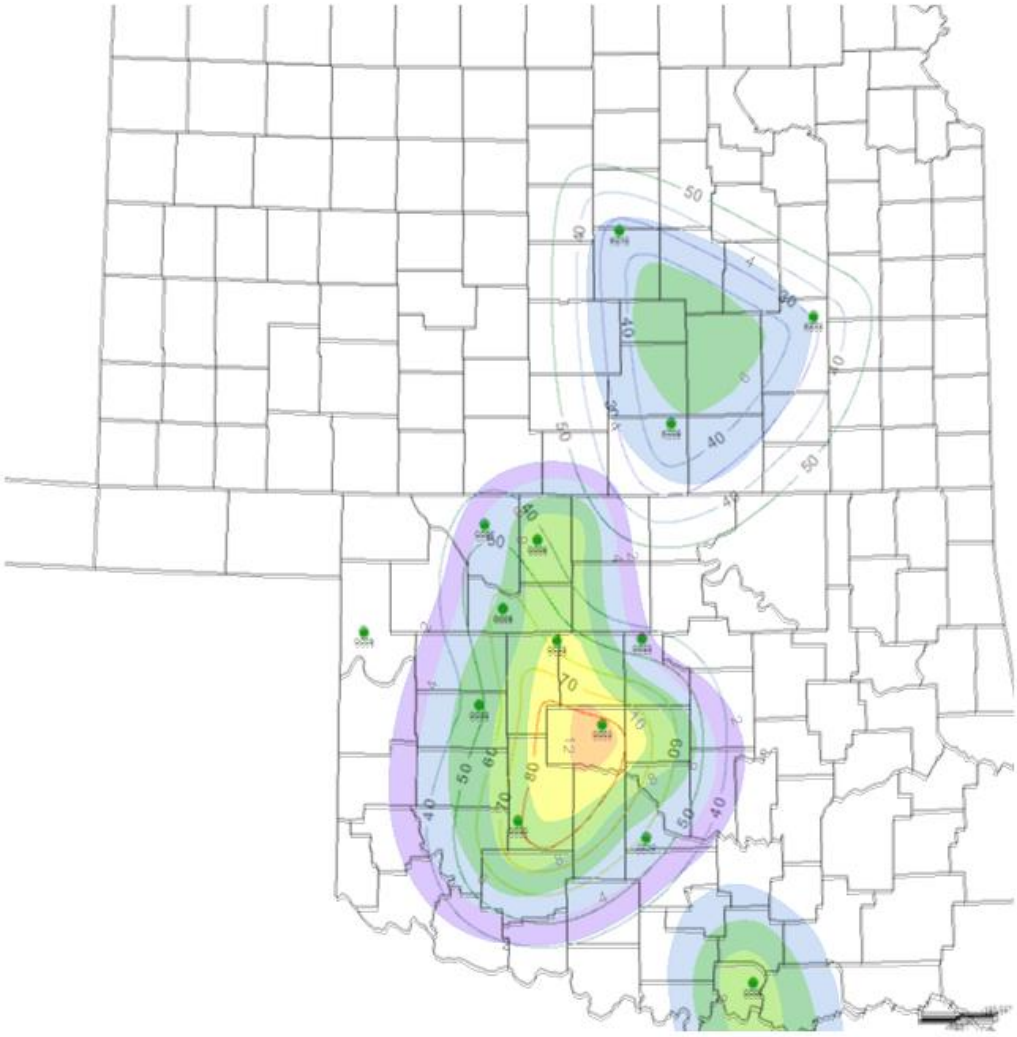

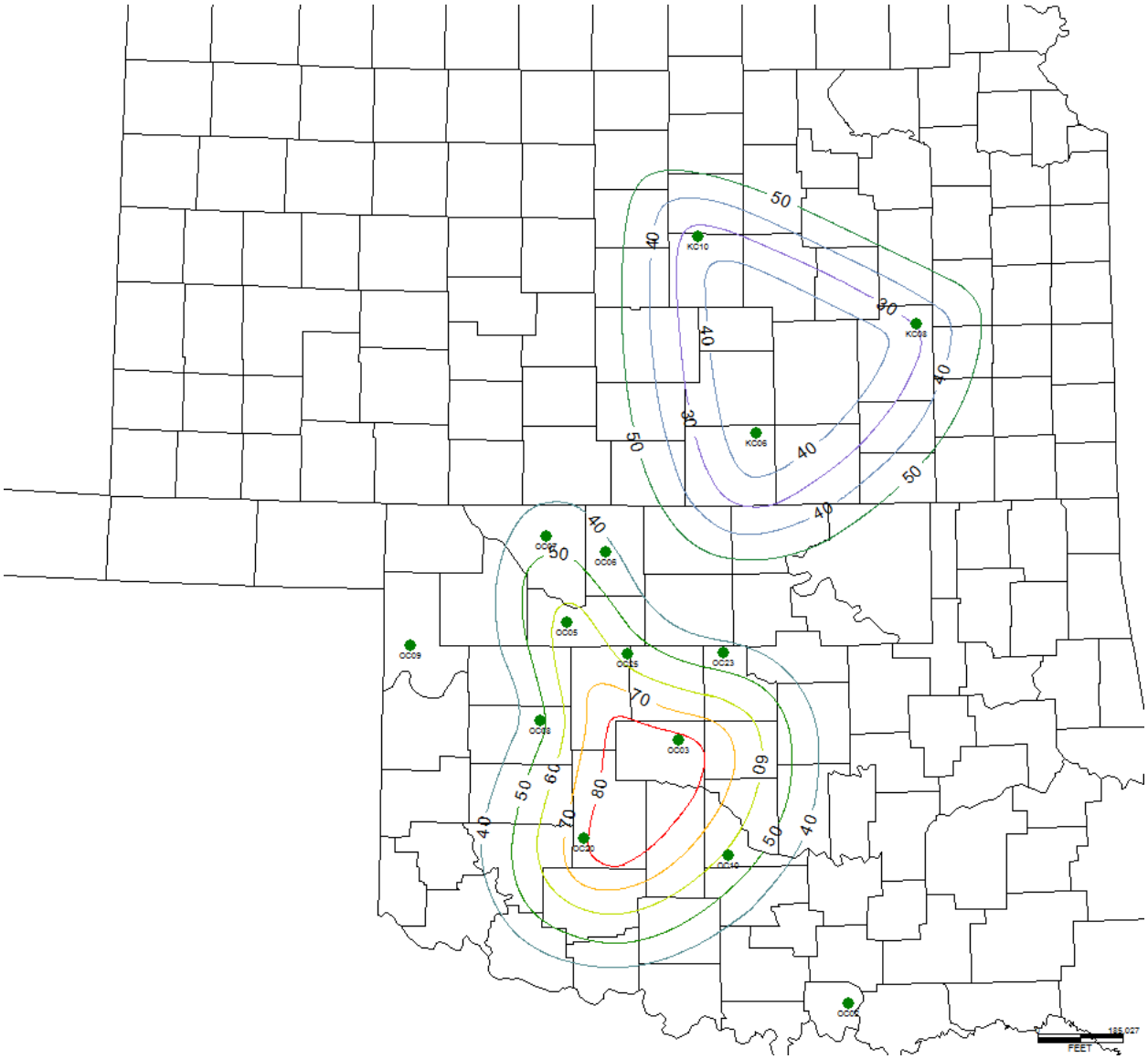

Figure A-13. Mineral based brittleness index contour map of Anadarko Basin based on evaluation of 13 cores.

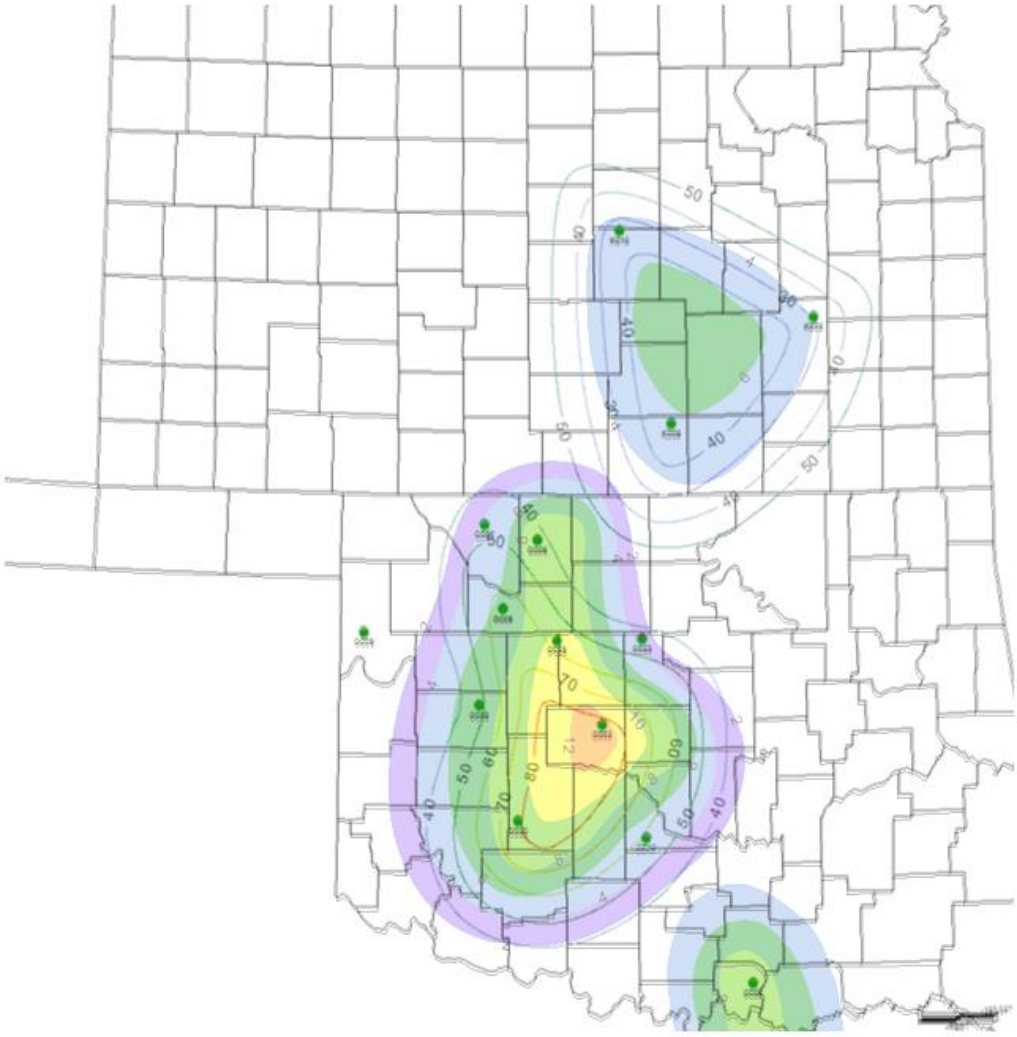

Figure A-14. Correlation of elastic and mineral based brittleness index contour maps depicting the most brittle regions of the basin.

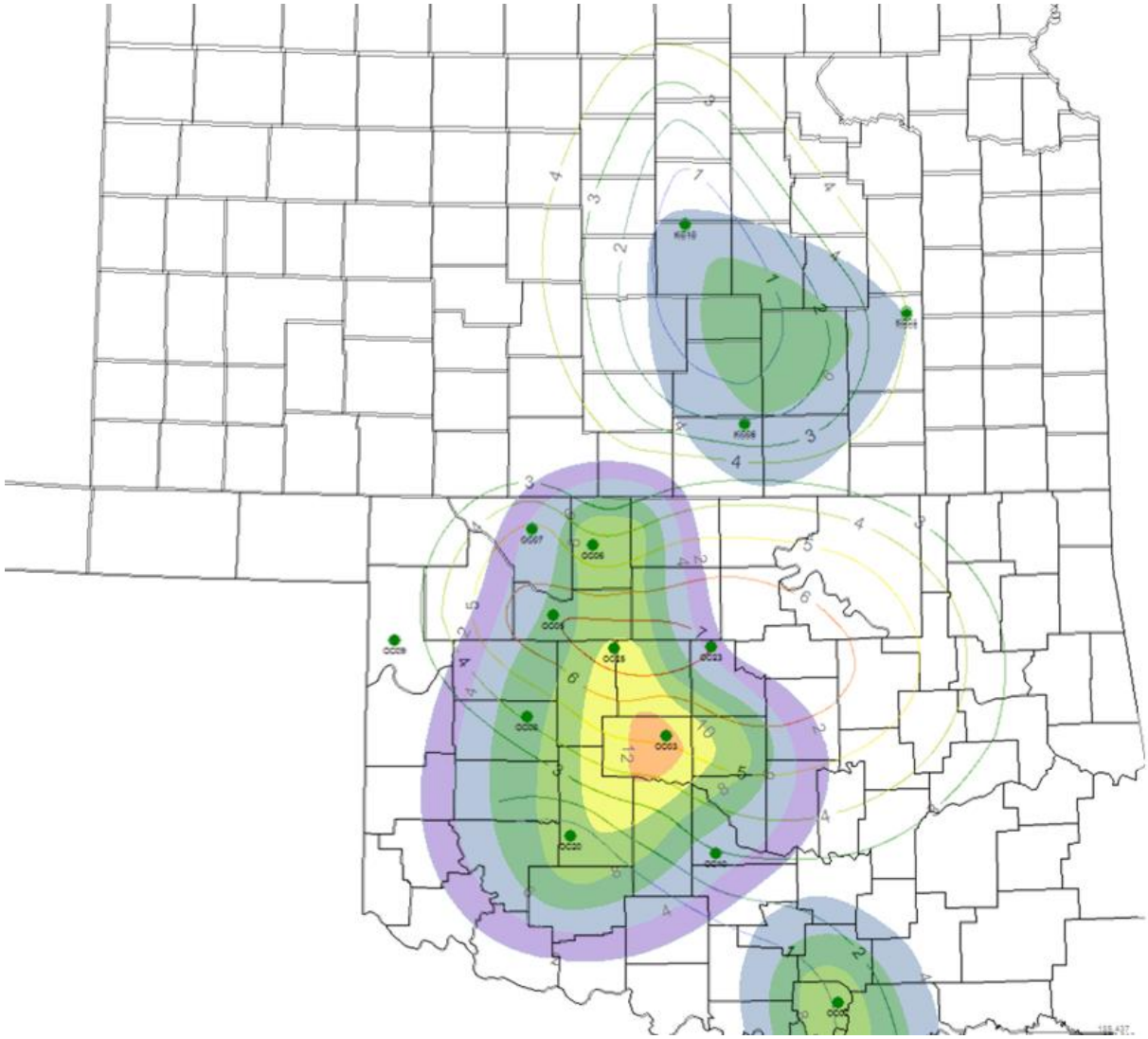

Figure A-14. Correlation of TOC and elastic brittleness contour maps